

## Infrared spectroscopic study of the dressed rotations of $\text{CN}^-$ isotopes in alkali halide crystals

C. E. Mungan, R. C. Spitzer,\* J. P. Sethna, and A. J. Sievers

*Laboratory of Atomic and Solid State Physics and Materials Science Center, Cornell University, Ithaca, New York 14853-2501*

(Received 19 July 1990)

High-resolution infrared absorption spectroscopy has been used to study the roto-vibrational spectra of cyanide ions doped into KCl for the two isotopes  $^{12}\text{C}^{14}\text{N}^-$  and  $^{13}\text{C}^{15}\text{N}^-$  in the temperature range 1.7–300 K. At the lowest temperature studied, new structure has been resolved in the spectra for low dopant concentrations (0.01 mol %). This structure is observed to merge into a single peak when strains are introduced into the crystal, confirming the association of these lines with tunneling by isolated cyanide ions. The structure is only partially explained by the Devonshire potential. Above 100 K, the isotopic variation in the experimental data is quantified in terms of a single global parameter, an integrated ratio of the widths of the entire roto-vibrational manifolds for the two isotopes, at each temperature. The values of this parameter turn out to be much smaller than what is predicted by a straightforward model of a cyanide dipole freely rotating in a crystalline host, but are consistent with a dressed-rotor model. By allowing a rotating cyanide ion to elastically distort the equilibrium structure of the surrounding lattice, and by using an adiabatic approximation and suitable averaging procedures, it is explicitly shown that an enhanced value for the moment of inertia of the dipole results. This model is fitted to the KCl:K  $^{12}\text{C}^{14}\text{N}$  spectra with the following free parameters: the rotational constant (in both the ground and excited vibrational levels), the Devonshire-potential-barrier parameter, and the widths of the roto-vibrational lines, with the result that the computed isotope effect is in good agreement with the experimental values. The best-fit values for these fitting parameters are found to be temperature dependent; the dressed moment of inertia of the  $\text{CN}^-$  ion increases with increasing temperature, in contrast to a naive expectation that the rotor should become more nearly free as the average lattice cage size increases. In similar fashion, for the fits to the room-temperature spectra measured for cyanide doped in eight other alkali halide hosts, the dressed moment of inertia tends, on average, to increase with increasing lattice spacing. Our model correctly predicts this trend in the data, although it fails to explain the observed magnitude of the effect. Furthermore, even after allowing these parameters to vary with temperature, detailed agreement between theory and experiment for the roto-vibrational manifold shape was not obtained.

### I. INTRODUCTION

In the past, the isolated cyanide ion doped into alkali halide hosts was studied extensively because it provided a simple but important model system for testing theories of the motion of matrix-isolated impurities (cf., Ref. 1 and references therein). The  $\text{CN}^-$  defect exhibits tunneling, librational, rotational, and vibrational modes of motion which have been studied by a large variety of techniques.<sup>2–10</sup> For KCl or KBr hosts, Seward and Narayanamurti<sup>2</sup> observed (at temperatures above 60 K) a broad double-humped spectrum centered at the fundamental transition of the stretch vibrational mode of the  $\text{CN}^-$  ion. Although the individual rotational components were not resolved, they interpreted this spectrum as arising from transitions within a rotational-vibrational manifold of levels of the freely rotating defect, in analogy with the spectra of gaseous diatomic molecules.<sup>11</sup>

Renewed interest in the vibrational dynamics of the cyanide-doped alkali halide system stems from the discovery of fluorescence from the vibrational transitions of the ion, initially with the molecule situated near an excited  $F$  center<sup>12</sup> and later with it isolated in the lattice.<sup>13</sup> This discovery subsequently led to the first observation of

lasing from the vibrational transitions of a molecular defect in the solid state.<sup>14</sup> Recent searches for other matrix-isolated ionic species that fluoresce and lase have turned up null results, despite the fact that the vibrational frequencies of these defects are much greater than the host phonon and defect rotational frequencies.<sup>15</sup> A conclusion from this is that all of the important energy decay channels of defect vibrational modes have not yet been identified. These results motivated us to return to the cyanide system and study, in detail, the nature of the defect-host-lattice coupling.

Analysis by Seward and Narayanamurti resulted in values for the rotational constant<sup>11</sup> of  $1.25 \text{ cm}^{-1}$  for KCl:CN<sup>-</sup> and  $1.0 \text{ cm}^{-1}$  for KBr:CN<sup>-</sup>, considerably smaller than the value ( $1.94 \text{ cm}^{-1}$ ) calculated for a bare cyanide ion. Other researchers<sup>3,16</sup> have confirmed a small value for the rotational constant, providing evidence that the ellipsoidal cyanide ion locally distorts the host lattice. Since these distortions should follow the rotating dipole, this coupling could lead to an increased effective moment of inertia and hence to a lower value for the rotational constant;<sup>16–20</sup> however, no attempt has been made to quantify this hypothesis and test its predictions with experiment.

In this paper, new experimental measurements are described which quantify the dependence of the rotational structure in the KCl:KCN spectra on the cyanide isotope. This effect could not be measured by previous researchers due to a lack of sensitivity. As expected, the results are not consistent with a free-rotor model, leading us to develop a physically intuitive model of a "dressed" roto-vibrator. The model consists in coupling the elastic dipole moment of the rotating cyanide ion to its nearest-neighboring host-lattice alkali ions. In the adiabatic approximation, these ions are permitted to relax instantaneously, producing an increase in the effective moment of inertia of the cyanide dipole, as compared to the free value.

We have applied this model to a systematic reanalysis of the experimental data as a function of host lattice (for nine different crystals) and, in one case (KCl:KCN), as a function of temperature. New values for the physically significant parameters are obtained, such as the rotational constant and the potential barrier height for KCl:KCN. In the case of this particular system, new structure has also been resolved in the tunneling spectrum at low concentration and temperature, structure which, in the main, is consistent with our dressed-rotor model. The overall picture of a matrix-isolated cyanide ion reorienting by rotating, librating, or tunneling, depending upon the temperature of the system and upon both a static crystal-field potential energy and a dynamic dressing contribution to the kinetic energy is found to qualitatively explain the ir spectroscopic data but such a picture is found, however, not to account for the detailed shape of the roto-vibrational manifold.

The outline of the paper is as follows. After a brief summary of the experimental techniques in Sec. II, the experimental results are presented in Sec. III in three parts: isotopic and temperature dependences of the KCl:KCN spectra, followed by room-temperature (RT) results for cyanide doped into eight other alkali halide hosts. Section IV concerns theory and its comparison with experiment. In Sec. IV A we develop the dressed-rotor model. This is subsequently applied to the cases of KCl and to the other alkali halide hosts investigated in subsections B and C, respectively. A discussion of the results is given in Sec. V. The paper ends with a brief summary. Three appendices follow. Appendix A gives a brief review of the free-rotor model, defining notation used in this paper, Appendix B treats the elastic coupling term in the dressed-rotor model, and, finally, Appendix C reviews the solution of Schrödinger's equation for the Devonshire potential.<sup>21</sup>

## II. EXPERIMENTAL TECHNIQUES

Infrared absorption spectra in the vicinity of the fundamental stretching mode  $\nu_0$  for cyanide (i.e., near 2000  $\text{cm}^{-1}$ ) were collected using a Bruker IR98 Fourier-transform interferometer (FTIR) at 1- $\text{cm}^{-1}$  resolution (unless otherwise noted) for runs at or above 50 K and 0.04  $\text{cm}^{-1}$  at lower temperatures. Sufficient signal-to-noise resolution was obtained in the high-temperature spectra by averaging together at least 500 interferograms

per run. In order to test the reproducibility of the data, several spectra were collected for each sample at each temperature of interest.

A Janis model 10DT Supervaritemp cryostat with ZnSe inner and NaCl outer windows was used for measurements below room temperature. Below 100 K, the sample temperatures were measured using a calibrated 1- $\text{k}\Omega$  Allen-Bradley resistor. Temperatures between 100 K and RT were measured using a type-J (iron-constantan) thermocouple. For the spectra used in the  $\text{CN}^-$  isotope study, it was important that the two samples of different isotopic composition be run at identical temperature. We therefore took special precautions to calibrate the thermocouple (consisting of two active junctions, one glued to the side of each sample) and to allow the sample chamber of the cryostat to reach a stable operating temperature. The sample temperatures were controlled using a Cryo T-2000 proportional-integral-differential temperature controller, using a silicon diode as a sensor and whose output was connected to a 75- $\Omega$  wire heater wrapped around the inlet capillary through which the cold helium entered the sample chamber. The temperature of each sample was individually controlled, so as to correct for a slight temperature gradient at the bottom of the cryostat (measured to be about one-third of a degree between the two samples). We estimated the temperature stability of a sample during a run at or above 100 K to be better than  $\pm 0.1$  K.

Room-temperature measurements were performed by suspending the samples directly in the vacuum space inside the interferometer. Again, when precise operating temperatures were required, the samples were allowed to thermally equilibrate with the thermostatted interior of the FTIR, a couple of degrees above the room's ambient temperature.

All of the boules were grown by the Czochralski method at Cornell University's Crystal Growing Facility under an atmosphere of argon. The actual  $\text{CN}^-$  concentration  $n$  ( $\text{in cm}^{-3}$ ) of any particular sample can be found using the relation<sup>2</sup>

$$n = \sigma^{-1} \alpha_{\text{peak}}, \quad (1)$$

where  $\alpha_{\text{peak}}$  is the peak value of the absorption coefficient ( $\text{in cm}^{-1}$ ) of the reflection-corrected cyanide spectrum (i.e., the  $R$ -branch peak height), and the inverse cross section  $\sigma^{-1}$  ( $\text{in cm}^{-2}$ ) at RT is given in Ref. 2 for the cases of KCl, KBr, KI, and RbCl, as determined by comparing the ir spectra to the results of chemical analyses. In particular, for KCl it has the value  $(3.6 \pm 0.4) \times 10^{19} \text{ cm}^{-2}$ .

## III. EXPERIMENTAL RESULTS

### A. KCl:KCN—Isotopic dependence

In Figs. 1(a) and 1(b), we present the reflection-corrected ir absorption spectra of a sample of KCl: $\text{K}^{12}\text{C}^{14}\text{N}$  and of KCl: $\text{K}^{13}\text{C}^{15}\text{N}$  for a number of temperatures between 100 K and RT. The concentration of cyanide in the crystals was small (0.054 and 0.052 mol %, respectively), so that the individual  $\text{CN}^-$  ions were, on average, well isolated from one another in the

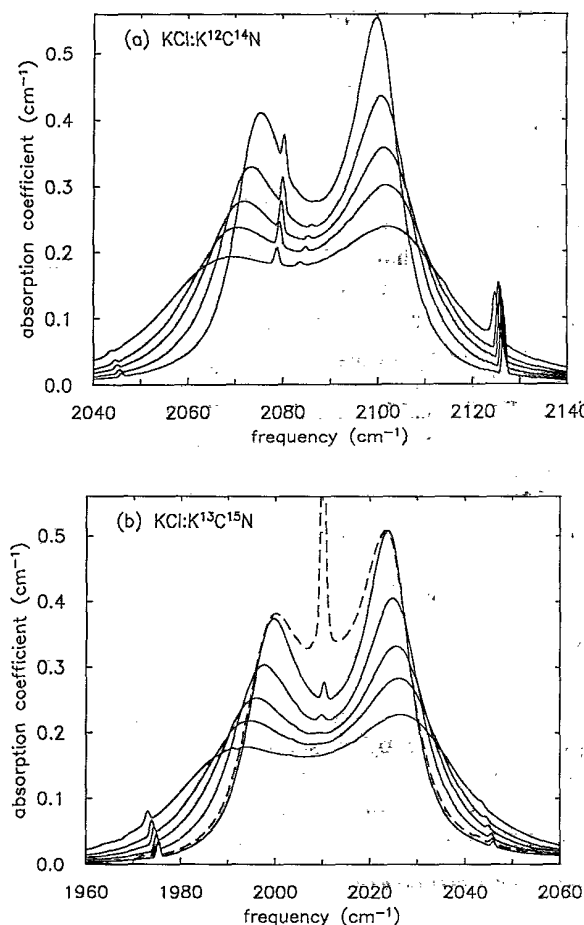


FIG. 1. Reflection-corrected absorption spectra for (a) KCl:K<sup>12</sup>C<sup>14</sup>N, and (b) KCl:K<sup>13</sup>C<sup>15</sup>N. The temperatures of the runs (solid curves) from top to bottom are 100, 140, 180, 220, and 297.1 K (RT). The <sup>12</sup>C<sup>14</sup>N<sup>-</sup> sample had a molar concentration of 0.054%, whereas the <sup>13</sup>C<sup>15</sup>N<sup>-</sup> sample concentration was 0.052%. The dashed curve in (b) shows the spectrum of a 0.39-mol % concentration <sup>13</sup>C<sup>15</sup>N<sup>-</sup> sample at 100 K, whose ordinate has been scaled so that its R peak height agrees with that of the 0.052% concentration <sup>13</sup>C<sup>15</sup>N<sup>-</sup> spectrum at 100 K.

lattice. In this high-temperature regime, the characteristic two-humped roto-vibrational spectrum is observed. Even at 0.04-cm<sup>-1</sup> resolution, no fine structure was observed in these spectra, in sharp contrast to the situation for gaseous HCN,<sup>22</sup> say, where a sequence of reasonably narrow lines composes each of the two branches since the roto-vibrational linewidths are much smaller than the spacing between adjacent lines (cf. Appendix A).

The sharp lines in the spectra do not arise from isolated cyanide ions but rather as follows. In the <sup>12</sup>C<sup>14</sup>N<sup>-</sup> spectra in Fig. 1(a), the weak line near 2045 cm<sup>-1</sup> is the  $\nu_3$  stretching mode<sup>23</sup> of <sup>10</sup>BO<sub>2</sub><sup>-</sup>, the two lines in the trough region are Na<sup>+</sup>:<sup>12</sup>C<sup>14</sup>N<sup>-</sup> combination modes, presumably for two different neighboring configurations of the sodium and the cyanide ions (this was determined by examining the spectra of a doubly doped KCl:KCN:NaCl sample), finally, the line near 2125 cm<sup>-1</sup> is the  $\nu_3$  stretching mode<sup>24</sup> of <sup>14</sup>N<sup>13</sup>C<sup>16</sup>O<sup>-</sup>. In the <sup>13</sup>C<sup>15</sup>N<sup>-</sup> spectra in Fig. 1(b), there again appears the

<sup>10</sup>BO<sub>2</sub><sup>-</sup> mode, as well as the <sup>11</sup>BO<sub>2</sub><sup>-</sup> stretching mode<sup>23</sup> at about 1975 cm<sup>-1</sup>. The strongly temperature-dependent line in the center of the trough region of the lower temperature <sup>13</sup>C<sup>15</sup>N<sup>-</sup> spectra is tentatively assigned to the <sup>13</sup>C<sup>15</sup>N<sup>-</sup>:<sup>13</sup>C<sup>15</sup>N<sup>-</sup> pair mode.<sup>25</sup>

The integrated strengths of the spectra for both isotopes are 15–16 cm<sup>-2</sup>, constant to within about 10% as a function of temperature. (This constancy could be verified all the way down to 1.7 K for the case of a 0.01-mol % <sup>12</sup>C<sup>14</sup>N<sup>-</sup> sample.) The <sup>12</sup>C<sup>14</sup>N<sup>-</sup> strengths are, however, about 10% larger than the corresponding <sup>13</sup>C<sup>15</sup>N<sup>-</sup> strengths, due presumably to the slightly higher cyanide concentration of the former and to the presence of the defect lines.

The present study represents the first systematic investigation of the ir spectra for the <sup>13</sup>C<sup>15</sup>N<sup>-</sup> isotope of cyanide. One can see in Fig. 1(b) that the <sup>13</sup>C<sup>15</sup>N<sup>-</sup> spectra are shifted downwards in frequency as a whole, compared to the <sup>12</sup>C<sup>14</sup>N<sup>-</sup> spectra in Fig. 1(a). Furthermore, when a <sup>13</sup>C<sup>15</sup>N<sup>-</sup> spectrum at some temperature is carefully overlaid on top of the corresponding <sup>12</sup>C<sup>14</sup>N<sup>-</sup> spectrum at the same temperature, it can be seen that the <sup>13</sup>C<sup>15</sup>N<sup>-</sup> manifold width is slightly smaller than that of the <sup>12</sup>C<sup>14</sup>N<sup>-</sup> spectrum.

Both of these effects can be understood in terms of the difference in masses of the two isotopes. First of all, the frequency shift of the vibrational stretch  $\nu_0$  is well known,<sup>26</sup> varying with the reduced mass  $\mu$  of the cyanide ion. To be specific, using the numbers listed in Table V (cf. Appendix A), we compute

$$[\mu(^{13}\text{C}^{15}\text{N}^-)/\mu(^{12}\text{C}^{14}\text{N}^-)]^{1/2} = 1.0382 ,$$

which is a little larger than the measured frequency shift (at 1.7 K),

$$\nu_0(\text{KCl: } ^{12}\text{C}^{14}\text{N}^-)/\nu_0(\text{KCl: } ^{13}\text{C}^{15}\text{N}^-) = 1.0378 .$$

This is consistent with a picture wherein the surrounding lattice ions participate slightly in the stretching motion of the dipole.

Secondly, the variation in the spectral widths with the isotopic masses arises because the individual roto-vibrational lines are spaced at frequency intervals of approximately  $2B_0$  in the free-rotor model (cf. Appendix A). But the rotational constant  $B_0 \propto I_0^{-1} \propto \mu^{-1}$  and hence the spectral width will decrease as the cyanide mass increases.

A more quantitative comparison of the predictions of the free-rotor model with the experimental data can be made. First, an estimate of the ratio of the spectral widths is calculated from the peak-to-peak separations of the P and R branches. We call this ratio  $s_{\text{free}}$  in the free-rotor model for the two different isotopes at a given temperature. The Boltzmann factor is used to calculate the relative rotational level populations and hence the value of the rotational quantum number  $J$  (call it  $J_{\max}$ ) which corresponds to the level of maximum population. This value is then inserted into Eq. (A1) for the transition frequencies, and the two frequencies  $\nu(0, J_{\max} - 1; 0, J_{\max})$  and  $\nu(0, J_{\max} + 1; 0, J_{\max})$  are calculated. The difference between these two frequencies is defined to be  $\Delta\nu_{PR}^{\max}$  and

is found to be equal to

$$\Delta\nu_{PR}^{\max} = (8B_0 kT / hc)^{1/2}, \quad (2)$$

ignoring the slight difference in value between  $B_1$  and  $B_0$  and allowing, if necessary, nonintegral values for  $J_{\max}$ . Taking this to be a rough measure of the predicted spectral width, then, at any given fixed temperature for both isotopes, we have

$$\begin{aligned} s_{\text{free}} &\approx \frac{\Delta\nu_{PR}^{\max}(^{12}\text{C}^{14}\text{N}^-)}{\Delta\nu_{PR}^{\max}(^{13}\text{C}^{15}\text{N}^-)} \\ &= \left[ \frac{I_0(^{13}\text{C}^{15}\text{N}^-)}{I_0(^{12}\text{C}^{14}\text{N}^-)} \right]^{1/2} = 1.038, \end{aligned} \quad (3)$$

which has been plotted in Fig. 2 as the line labeled "free rotor."

In order to minimize the errors associated with finding the experimental values  $s_{\text{exp}}$  [e.g., we cannot measure the peak-to-peak separations or full widths at half maximum (FWHM) to better than about  $\pm 5\%$ ], and in order to avoid making any assumptions regarding what feature (e.g., the FWHM, the peak-to-peak separation, the extent of the wings of the spectra) of the data best characterizes a spectrum's "width," we have adopted the following general method of analysis, which takes maximum advantage of the data.

Two spectra due to the different isotopes (at identical temperature) are overlaid onto each other and the width of the higher-mass spectrum is stretched until its shape best agrees with the shape of the lower-mass spectrum. In practice, this is done by numerically minimizing the

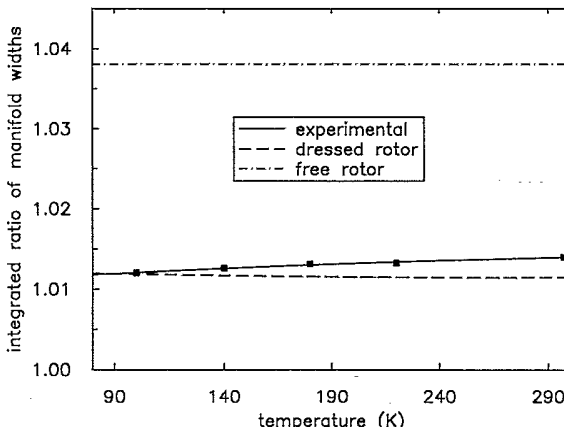


FIG. 2. Comparison of the experimental values of the isotope parameter  $s_{\text{exp}}$  (which is an integrated ratio of the roto-vibrational manifold widths of the  $^{12}\text{C}^{14}\text{N}^-$  spectra to those of the  $^{13}\text{C}^{15}\text{N}^-$  spectra) with the theoretical predictions of the free-rotor ( $s_{\text{free}}$ ) and dressed-rotor ( $s_{\text{dressed}}$ ) models. The heights of the squares representing the experimental data are roughly equal to the size of the error bars for one standard deviation variance in the mean values obtained by averaging together numerous runs. The solid line through the experimental points is a guide to the eye.

overlap integral (that is, the area between the two curves),

$$\int_{\nu_{\text{start}}}^{\nu_{\text{stop}}} \left| \frac{\alpha_1(s_{\text{exp}}\nu)}{\alpha_{1 \text{ peak}}} - \frac{\alpha_2(\nu - \Delta\nu)}{\alpha_{2 \text{ peak}}} \right| d\nu, \quad (4)$$

as a function of the two variables  $s_{\text{exp}}$  and  $\Delta\nu$ , where  $\alpha_1(\nu)$  is the absorption coefficient of the lower-mass spectrum and  $\alpha_2(\nu)$  is that of the higher-mass spectrum. (Explicitly subtracting out the extraneous, sharp, impurity lines in the spectra produced negligible changes in the values obtained for  $s_{\text{exp}}$ .) The cutoffs  $\nu_{\text{start}}$  and  $\nu_{\text{stop}}$  are not critical; we chose these limits to correspond to that portion of the spectrum having an absorption coefficient exceeding 30% of the peak value so as to minimize noise and background effects. The frequency shift  $\Delta\nu$  merely keeps the spectra overlaid on top of each other, whereas  $s_{\text{exp}}$  is the parameter of interest. One can see from Eq. (4) that it represents an integrated ratio of the manifold widths for the two isotopes. The resulting values have been plotted as solid squares in Fig. 2.

The temperature precision required to obtain these experimental values should be emphasized. By fixing the temperature of one sample at 180.0 K and varying the temperature of the other sample by small increments about this value, we found that the values for  $s_{\text{exp}}$  obtained using Eq. (4) vary linearly with the temperature difference between the samples, with a slope

$$\Delta s_{\text{exp}}/\Delta T \approx 0.003/\text{K}.$$

In other words, the error bars on the experimental data in Fig. 2 represent an averaged stability and match between the temperatures of the two samples on the order of  $\pm 0.1$  K.

As a check,  $s_{\text{exp}}$  was computed in this same way for pairs of spectra of the same isotope at each temperature. Any runs which, when compared to other runs, gave values of  $s_{\text{exp}}$  differing from unity by more than  $\pm 0.0005$  were discarded.

### B. KCl:KCN—Temperature dependence

In Fig. 3, the absorption spectra for KCl:K  $^{12}\text{C}^{14}\text{N}$  for a range of temperatures has been plotted. With decreasing temperature, the spectral width decreases and the center frequency  $\nu_0$  increases. The former effect arises because of declining thermal populations of the higher rotational levels, as reflected by the Boltzmann factor, as in Eq. (A8). The shift in the center frequency is linear in temperature ( $\sim 0.005 \text{ cm}^{-1}/\text{K}$ ) and can be understood<sup>26</sup> on the basis of phonon-scattering processes and thermal contraction of the lattice.

At the lowest temperatures, a  $Q$  branch grows up out of the trough region of the spectra with the onset<sup>2</sup> occurring at a fairly precise temperature between 55 and 60 K. This fact places a strong restriction on the size of the ratio of the reorientational potential barrier height to the rotational constant.

Only the smooth  $P$ ,  $Q$ , and  $R$  branches (ignoring some sharp cyanide-defect combination lines, most of which have been subtracted out of the spectra for the sake of

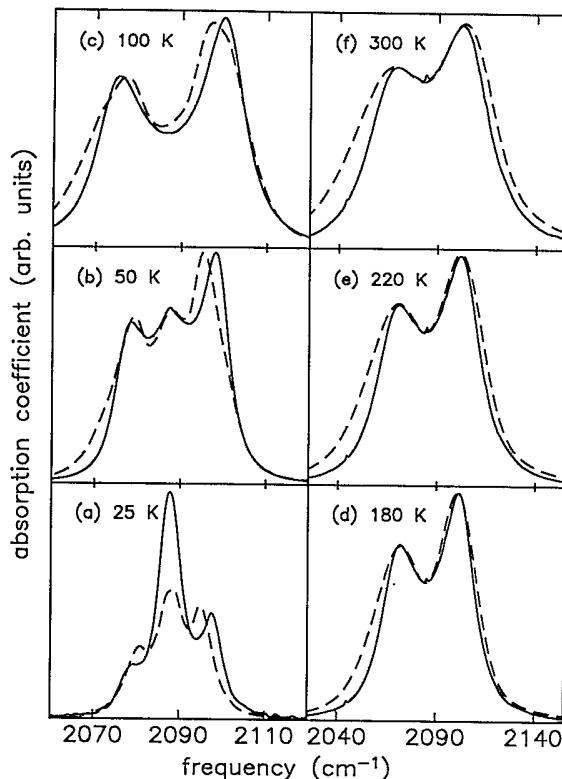


FIG. 3. Reflection-corrected absorption spectra (solid curves) for KCl:K<sup>12</sup>C<sup>14</sup>N as a function of temperature. Note the different horizontal scale used for the left-hand side of the figure, as compared to the right-hand side. The sample concentrations were 0.052 mol % except at 25 K, where a 0.01% sample was used. The resolutions were 1 cm<sup>-1</sup>, except at 25 K, where a resolution of 0.04 cm<sup>-1</sup> was used, showing that no fine structure exists in this spectrum. The dashed curves are fits to the dressed-rotor model using  $B_0^* = 0.60 \text{ cm}^{-1}$ ,  $B_1^* = 0.592 \text{ cm}^{-1}$ , and  $K = -15 \text{ cm}^{-1}$ . The linewidths (FWHM)  $\gamma_0$  and  $\gamma_\infty$  used in the fits, and the temperatures of the runs were as follows: (a) 25 K ( $\gamma_0 = 2.8 \text{ cm}^{-1}$ ,  $\gamma_\infty = 2.8 \text{ cm}^{-1}$ ), (b) 50 K ( $\gamma_0 = 4.4 \text{ cm}^{-1}$ ,  $\gamma_\infty = 3.4 \text{ cm}^{-1}$ ), (c) 100 K ( $\gamma_0 = 8.8 \text{ cm}^{-1}$ ,  $\gamma_\infty = 4.4 \text{ cm}^{-1}$ ), (d) 180 K ( $\gamma_0 = 18.0 \text{ cm}^{-1}$ ,  $\gamma_\infty = 8.0 \text{ cm}^{-1}$ ), (e) 220 K ( $\gamma_0 = 24.0 \text{ cm}^{-1}$ ,  $\gamma_\infty = 10.0 \text{ cm}^{-1}$ ), and (f) 297.1 K ( $\gamma_0 = 34.0 \text{ cm}^{-1}$ ,  $\gamma_\infty = 14.0 \text{ cm}^{-1}$ ). Also see Fig. 8 for the case of 140 K.

clarity) are seen in the spectra in Fig. 3. The situation changes however at yet lower temperatures. In Fig. 4, spectra at 1.7 K are shown for very-low-concentration (0.01 mol %) KCl:K<sup>12</sup>C<sup>14</sup>N (solid line) and KCl:K<sup>13</sup>C<sup>15</sup>N (dashed line) samples. The inset shows the high-frequency sidebands with a compressed frequency scale. For comparison, we have shifted the KCl:K<sup>13</sup>C<sup>15</sup>N spectrum to higher frequency by 75.96 cm<sup>-1</sup> and multiplied its ordinate by a scaling factor of 1.18. At higher sample concentrations, the central features located at about 2087.5 cm<sup>-1</sup> in the figure (which could either be nontunneling centers or cyanide-impurity combination modes) increase dramatically in strength, blurring the tunnel splitting, and the librational sideband broadens and shifts to higher frequencies.

The spectra for both isotopes in Fig. 4 consist of three principal sets of lines. For the case of KCl:K<sup>12</sup>C<sup>14</sup>N in

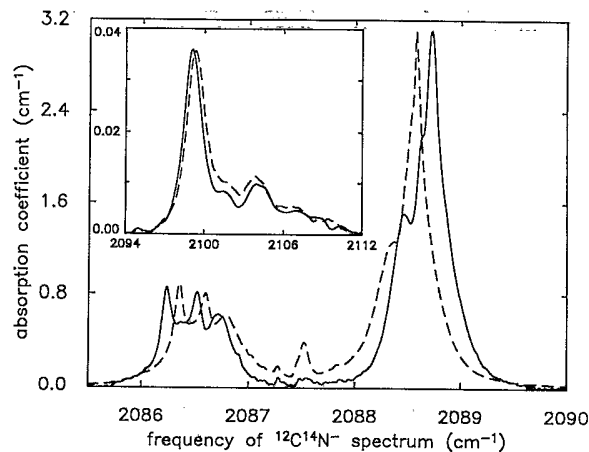


FIG. 4. Reflection-corrected absorption spectra for nominally 0.01-mol % KCl:K<sup>12</sup>C<sup>14</sup>N (solid curve) and KCl:K<sup>13</sup>C<sup>15</sup>N (dashed curve) samples at 1.7 K and 0.04-cm<sup>-1</sup> resolution. (The KCl:K<sup>13</sup>C<sup>15</sup>N spectrum has been shifted upwards in frequency by 75.96 cm<sup>-1</sup> and has been scaled vertically by a factor of 1.18 for the purposes of comparison with the KCl:K<sup>12</sup>C<sup>14</sup>N spectrum.) The two sets of lines in the main plot peaked at  $2086.5 \pm 0.1 \text{ cm}^{-1}$  and  $2088.7 \pm 0.1 \text{ cm}^{-1}$  (for the <sup>12</sup>C<sup>14</sup>N<sup>-</sup> isotope) are the difference and sum tunneling bands, respectively, of the main vibrational stretching mode, split by  $1.05 \pm 0.05 \text{ cm}^{-1}$  from the center frequency  $\nu_0 = 2087.57 \pm 0.05 \text{ cm}^{-1}$ . The weak, broad peak in the inset plot (note the change of scales) at  $2099.1 \pm 0.1 \text{ cm}^{-1}$ , and the structure extending above it to higher frequencies, are the sum librational transitions.

order of decreasing strength these are centered at

$$+1.05 \pm 0.05 \text{ cm}^{-1} (\equiv \Delta\nu_{\text{tun}}), \\ -1.05 \pm 0.05 \text{ cm}^{-1},$$

and

$$+11.5 \pm 0.1 \text{ cm}^{-1} (\equiv \Delta\nu_{\text{lib}}),$$

relative to the frequency  $\nu_0 = 2087.57 \pm 0.05 \text{ cm}^{-1}$ . They are identified as tunneling sum transitions, tunneling difference transitions, and the lowest-order librational sum transitions, respectively. This nomenclature reflects the points of view of Hexter and Dows' librational model<sup>27</sup> and Gomez *et al.*'s tunneling model.<sup>28</sup> An alternative, but equivalent,<sup>4</sup> viewpoint is that of the Devonshire model,<sup>21</sup> whereby the tunneling and librational levels arise as perturbations of the free-rotor wave functions.

Inspection of the results in Fig. 4 show that the tunnel splitting  $\Delta\nu_{\text{tun}}$  of the heavier isotope has decreased by about  $0.10 \text{ cm}^{-1}$  and the librational splitting  $\Delta\nu_{\text{lib}}$  has increased by about  $0.20 \text{ cm}^{-1}$ , relative to the spectrum of the lighter isotope, but the two spectra are otherwise virtually identical.

In order to investigate the spectrum further, strains were deliberately introduced into the 0.01-mol % KCl:K<sup>12</sup>C<sup>14</sup>N sample by loading it with dislocations in a pellet press. In Fig. 5, we compare the low-temperature tunneling spectrum of this sample (dashed line) to the prior spectrum (solid line). We see that the tunneling sum

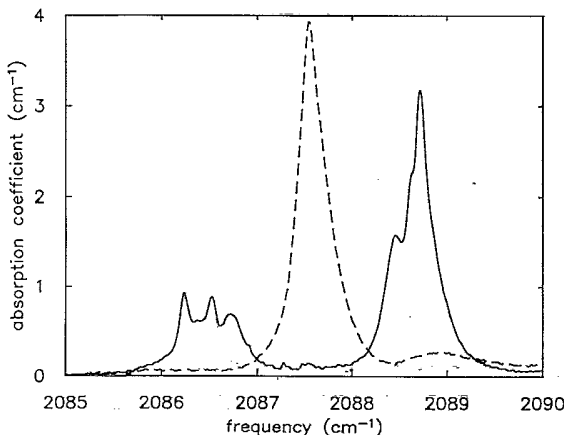


FIG. 5. Effect of dislocation-induced strains upon the KCl:K<sup>12</sup>C<sup>14</sup>N spectrum in the stretching mode frequency region. The solid curve is the tunnel split spectrum of Fig. 4. The dashed curve is the absorption spectrum for the same sample after introducing dislocations into it. For both spectra the sample temperature was 1.7 K and the spectral resolution was 0.04 cm<sup>-1</sup>. The integrated strengths of both spectra are identical, to within one-quarter of a percent.

and difference bands have almost completely disappeared and are replaced by a central asymmetric peak. The integrated line strengths of the two spectra are equal to each other, to within one-quarter of a percent. It appears that the strain fields associated with the dislocations destroy the equivalence of the potential wells so that tunneling no longer occurs and a single strain-broadened  $Q$  branch appears.<sup>29</sup> The effect of the strains upon the librational band is to cause it to shift to slightly higher frequencies and become broader and rounder in shape; strains produce a distribution of widths and depths of the

potential wells and these in turn determine the librational transition frequencies.

### C. CN<sup>-</sup> in other alkali halide hosts

Nine lattice combinations formed from K<sup>+</sup>, Rb<sup>+</sup>, or Cs<sup>+</sup> alkali ions, plus Cl<sup>-</sup>, Br<sup>-</sup>, or I<sup>-</sup> halides doped with CN<sup>-</sup> have been investigated. Some important empirical parameters for these nine systems are listed in Table I (together with the values of our fitting parameters, discussed later). The spectra of the sodium salts are known<sup>2,30</sup> to be very different from those of the above nine hosts and have not been included in the present study. Furthermore, only results at RT are presented in this paper.

In Fig. 6, the absorption spectra for the fundamental stretching mode regions of <sup>12</sup>C<sup>14</sup>N<sup>-</sup> doped into these nine hosts is shown. The cyanide concentration was roughly 0.5 mol % in all cases. No sample of cyanide-doped CsBr was available; the depicted spectrum was computed from a raw transmission spectrum plotted in Ref. 30.

A number of foreign impurities are apparent as sharp lines in the spectra: the difference between the solid and dashed traces at the high-frequency side of the spectra of the alkali iodides identifies the wing of the <sup>14</sup>N<sup>12</sup>C<sup>16</sup>O<sup>-</sup> peaks;<sup>24</sup> a narrow <sup>14</sup>N<sup>13</sup>C<sup>16</sup>O<sup>-</sup> peak (Ref. 24) appears on the right-hand edge of the spectra for the cases of KI, RbCl, RbI, CsCl, and CsI; the lines near the peaks of the RbCl, RbBr, CsCl, and CsI spectra are probably <sup>12</sup>C<sup>14</sup>N<sup>-</sup> in combination with Na<sup>+</sup> or some other alkali-metal ion; and finally, a <sup>10</sup>BO<sub>2</sub><sup>-</sup> peak<sup>23</sup> is located near the left-hand edge of the RbCl spectrum.

For any given alkali host series in Fig. 6, the spectral widths decrease with increasing lattice constant so that

TABLE I. Parameters of importance for cyanide doped into nine alkali halides. The lattice constants  $a$  were taken from Ashcroft and Mermin (Ref. 38, pp. 80–81). The shape factors ( $\lambda_1 - \lambda_2$ ) for the potassium salts were measured by Beyeler in  $\langle 110 \rangle$  stress-splitting experiments (Ref. 55); the value for the rubidium hosts was estimated by averaging together the values for the potassium hosts. The center frequencies  $\nu_0$  were obtained from the fits to the RT spectra in Fig. 6 with a fitting error of  $\pm 1$  cm<sup>-1</sup>. The room-temperature rotational constants  $B_0^*$  and  $B_1^*$  were also obtained from these fits; the errors were approximately  $\pm 0.02$  cm<sup>-1</sup> in  $B_0^*$  and  $\pm 1\%$  in the ratio  $B_1^*/B_0^*$ . The notation “NA” means that the data did not permit us to find a fitted value for  $B_1^*$ ; in such cases, we have used  $B_1^* = B_0^*$  in the fits in Fig. 6. The fitted FWHM ( $\gamma_0$  for lines near the center frequency and  $\gamma_\infty$  for lines in the wings of the spectra) are accurate to about  $\pm 10\%$ .

Host	$a$ (Å)	$(\lambda_1 - \lambda_2)$	$\nu_0$ (cm <sup>-1</sup> )	$B_0^*$ (cm <sup>-1</sup> )	$B_1^*$ (cm <sup>-1</sup> )	$\gamma_0$ (cm <sup>-1</sup> )	$\gamma_\infty$ (cm <sup>-1</sup> )
KCl	6.29	0.18	2087.0	0.47	0.463	36	12
KBr	6.60	0.20	2079.5	0.29	0.285	44	18
KI	7.07	0.27	2067.5	0.15	NA	28	34
RbCl	6.58	0.22	2079.0	0.15	NA	36	24
RbBr	6.85	0.22	2071.5	0.14	NA	30	28
RbI	7.34	0.22	2063.0	0.13	NA	24	34
CsCl	4.12		2075.0	0.23	NA	26	26
CsBr	4.29		2070.5	0.17	0.169	18	30
CsI	4.57		2054.5	0.15	NA	28	38

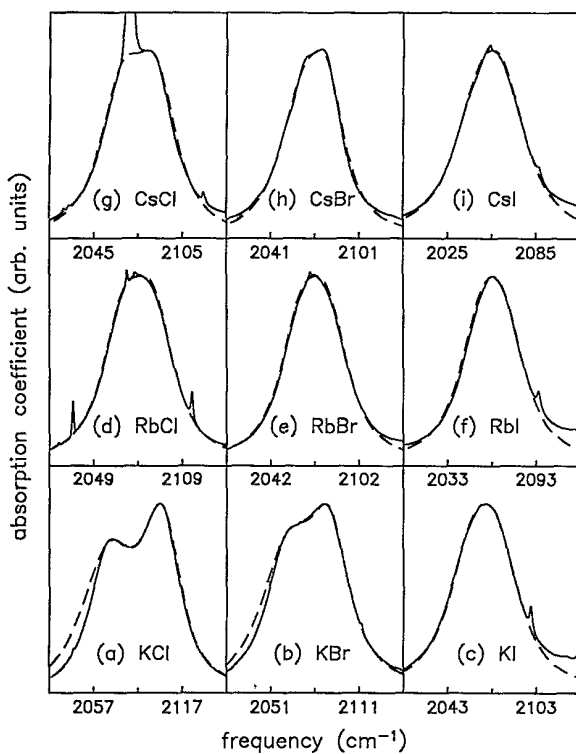


FIG. 6. Reflection-corrected absorption spectra (solid curves) at RT for cyanide doped into the indicated nine hosts with a nominal concentration of 0.5 mol %. The CsBr spectrum was computed from a transmission spectrum published in Ref. 30. Various impurities appear in these spectra as narrow lines, including the unusually strong one just below the peak of the CsCl:CN<sup>-</sup> spectrum (which is probably CN<sup>-</sup> plus Na<sup>+</sup>, K<sup>+</sup>, and/or Rb<sup>+</sup>). The dashed curves are fits to the dressed-rotor model using the values of  $\nu_0$ ,  $B_0^*$ ,  $B_1^*$ ,  $\gamma_0$ , and  $\gamma_\infty$  given in Table I.

the *P* and *R* branches quickly tend to overlap and blend together. This, in turn, implies that the dressed values of the rotational constants in each of the series decrease—i.e., are in increasing discrepancy with the free value  $B_0$ —with increasing lattice cage size.

#### IV. THEORY AND COMPARISON WITH EXPERIMENT

##### A. Dressed-rotor model

The basic idea<sup>16–19</sup> behind the model introduced here is that the cyanide ion locally distorts the lattice and drags these deformations around with it as it rotates. This results in an enhanced (or “dressed”) value for the effective moment of inertia of the ion. The distortions can, in general, be of two sorts: elastic interactions between the dipole and the lattice, and electric ones. Elastic deformations arise because the cyanide ion is ellipsoidal with<sup>31</sup> the length of its semimajor axis equal to 2.15 Å and that of its semiminor axis equal to 1.78 Å. Hence, the nearest-neighboring lattice ions along the symmetry axis of the dipole are pushed outwards, whereas those perpendicular to this axis are pulled inwards, as the dipole rotates. The electric term, on the other hand, is an interaction between the electric dipole

moment of the cyanide ion and the polar salt lattice. However, the contribution to the dressing of the moment of inertia of a CN<sup>-</sup> ion by the electric coupling term is much smaller than that of the elastic term<sup>32</sup> and has therefore been neglected in the following development.

We proceed to semiclassically quantify the elastic coupling between the cyanide dipole and the lattice ions.<sup>33</sup> The model can be understood by reference to the schematic in Fig. 7. We suppose, for the sake of specificity, that the host is KCl. (The model can be immediately generalized to the other NaCl-structure hosts; the CsCl-structure hosts require substantial, but straightforward, modifications in the ensuing discussion.) Let  $\beta_i$  represent the orientation of the CN<sup>-</sup> ion [in an octahedrally symmetric, static crystal potential  $V_s(\theta, \phi)$ ] with respect to the *i*th crystal axis, where the axes are chosen, as indicated, to lie along the ⟨100⟩ directions. In particular, using the numbering scheme in the figure, it can be seen that

$$\begin{aligned}\beta_1 &= \cos^{-1}(\cos\phi \sin\theta), \\ \beta_2 &= \theta, \\ \beta_3 &= 180^\circ - \beta_1, \\ \beta_4 &= 180^\circ - \theta, \\ \beta_5 &= 180^\circ - \beta_6, \\ \beta_6 &= \cos^{-1}(\sin\phi \sin\theta),\end{aligned}\quad (5)$$

where  $\phi$  and  $\theta$  are the conventional spherical polar angles

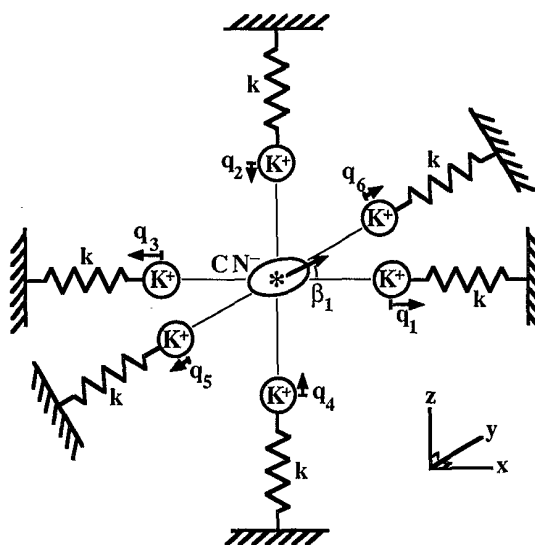


FIG. 7. Schematic model for the coupling between an ellipsoidal CN<sup>-</sup> ion (whose geometric center is located at the lattice site, indicated by the asterisk) and its nearest-neighboring alkali (in this case, K<sup>+</sup>) ions. These six alkali ions have been labeled 1–6 and have displacements  $q_i$  relative to their equilibrium sites in a perfect KCl crystal. They are coupled to the rest of the lattice (represented as being rigid) by springs (with spring constants  $k$ ). The cyanide ion has orientation  $\beta_i$  with respect to the *i*th crystal axis (for example,  $\beta_1$  is shown in the figure), where the coordinate system has been chosen to coincide with the ⟨100⟩ crystal axes, as indicated.

(defined with respect to the crystal axes). The displacement of the  $i$ th nearest-neighboring alkali ion (of mass  $m_K$ ), of which there are six in all, is given by  $q_i$ . Local vibrations of the lattice ions (as determined by the springs<sup>34</sup>  $k$ ) are elastically coupled to the rotation of the cyanide ion by two coupling constants,  $\xi_1$  and  $\xi_2$ , as shall be derived subsequently, which relate the orientation of the cyanide ion to the displacements of its nearest-neighboring potassium ions. One might not expect the center of mass of the cyanide ion to sit on center. A more likely situation would be to have the geometrical center of the dipole at the lattice site, thus minimizing the elastic interactions between the CN<sup>-</sup> dipole and its neighbors. This results in a displacement of the center of mass of the cyanide ion by a small amount, given by

$$\Delta r = \frac{1}{2}r \frac{m_N - m_C}{m_N + m_C}, \quad (6)$$

where  $r$  is the separation between the carbon and nitrogen atoms, contributing a term  $m_{CN}(\Delta r)^2$  to the moment of inertia. The classical Hamiltonian  $H$  of the system now follows as

---


$$H = \frac{1}{2}I'(\dot{\theta}^2 + \sin^2\theta \dot{\phi}^2) + 8m_K\xi_1^2[(1 - \cos^2\phi \sin^2\phi)\sin^2(2\theta)\dot{\theta}^2 + \sin^2(2\phi)\sin^4\theta \dot{\phi}^2 - \sin(4\phi)\cos\theta \sin^3\theta \dot{\phi}\dot{\theta}] + V_s(\theta, \phi) + V_d(\theta, \phi), \quad (9)$$


---

where  $V_d(\theta, \phi)$ , the *dynamic* contribution to the potential, is a function of  $\theta$ ,  $\phi$ ,  $\xi_1$ , and  $\xi_2$ . The sum of the first two expressions on the right-hand side of this equation represents the kinetic energy and results in an angle- and speed-dependent moment of inertia. In order to make the expression more tractable, we make the substitutions  $\dot{\theta} = \omega_{\text{rot}} \cos\rho$  and  $\sin\theta \dot{\phi} = \omega_{\text{rot}} \sin\rho$ , where  $\omega_{\text{rot}}$  is the average angular speed of the cyanide ions and  $\rho$  takes on values between 0° and 360°.

We now distinguish two temperature ranges for the purpose of analysis of the data: high temperatures, above about 60 K, where the motion of the cyanide ions is not greatly perturbed by the potential; and lower temperatures, where the ions are most likely to have orientations near those of the potential minima. Consider first the high-temperature regime. Since any real spectroscopic experiment will tend to probe a large number of cyanide ions, and since each ion will have a random instantaneous magnitude and direction of its angular velocity vector, we can find an effective moment of inertia  $I^*$  by averaging the kinetic energy in Eq.(9) over the three angles  $\theta$ ,  $\phi$ , and  $\rho$ .<sup>36</sup> This gives

$$\langle E_{\text{kin}} \rangle_{\theta, \phi, \rho} = \frac{1}{2}(I' + 6.40m_K\xi_1^2)\omega_{\text{rot}}^2 \equiv \frac{1}{2}I^*(T \rightarrow \infty)\omega_{\text{rot}}^2, \quad (10)$$

$$H = \frac{1}{2}I'(\dot{\theta}^2 + \sin^2\theta \dot{\phi}^2) + V_s(\theta, \phi) + \sum_{i=1}^6 \left\{ \frac{1}{2}m_K \dot{q}_i^2 + \frac{1}{2}kq_i^2 - kq_i[\xi_1 \cos(2\beta_i) + \xi_2] \right\}, \quad (7)$$

where  $I' \equiv I + m_{CN}(\Delta r)^2 = \frac{1}{4}(m_C + m_N)r^2$  and the signs in the coupling term have been chosen so that  $q_i > 0$  for displacements of the  $i$ th potassium ion away from the cyanide ion. In the adiabatic approximation, the lattice relaxes instantaneously in comparison to the relatively slow rotation of the cyanide ion.<sup>35</sup> Thus, values for  $q_i$  can be obtained by minimizing the Hamiltonian with respect to  $q_i$ , with  $\beta_i$  fixed, to obtain

$$q_i = \xi_1 \cos(2\beta_i) + \xi_2. \quad (8)$$

In Appendix B, the form of the coupling term (in  $\xi_1$  and  $\xi_2$ ) is determined by comparison with this expression for  $q_i$ .

Next, Eq. (8) is rewritten in terms of the spherical polar angles  $\theta$  and  $\phi$ , using Eq. (5), and differentiated with respect to time to find  $\dot{q}_i$ . Then,  $q_i$  and  $\dot{q}_i$  are substituted back into the Hamiltonian together with the formulas for  $\beta_i$ , and the summation is explicitly performed. This eliminates the lattice coordinates from the problem and one obtains

resulting in a larger value for the moment of inertia than the bare (free) value  $I$ .

Next, consider the low-temperature regime. To a good approximation we can now fix the values of  $\theta$  and  $\phi$  to correspond to any one of the equivalent orientations of the ⟨111⟩ potential well minima, say  $\phi = 45^\circ$  and  $\theta = \cos^{-1}(1/\sqrt{3})$ . Substituting these values into our expression for the kinetic energy gives

$$E_{\text{kin}}|_{\text{potential well}} = \frac{1}{2}(I' + 10.7m_K\xi_1^2)\omega_{\text{rot}}^2 \equiv \frac{1}{2}I^*(T \rightarrow 0)\omega_{\text{rot}}^2, \quad (11)$$

independent of the value of  $\rho$  (as expected on the basis of symmetry).

In either case, in analogy to Eq. (A5), we define the dressed rotational constant  $B^*$  of the system to be

$$B^* \equiv \frac{\hbar}{8\pi^2 c I^*}, \quad (12)$$

which is consequently expected to be temperature dependent. Using the value of  $\xi_1$  computed in Appendix B, one finds  $B^* = 1.36 \text{ cm}^{-1}$  at high temperatures and  $1.14 \text{ cm}^{-1}$  at low temperatures. These numerical results depend critically, however, on the assumptions and approxima-

tions upon which our model is based. In order to relax this constraint, in the following subsection, when we actually attempt to reproduce the experimental spectra, we decided to allow  $B^*$  to be a free-fitting parameter at each temperature.

Finally, the remaining two terms in Eq. (9) specify the orientational potential energy of the dressed rotor:

$$V_{\text{pot}} = V_s(\theta, \phi) + V_d(\theta, \phi). \quad (13)$$

This retains the octahedral symmetry of the undressed potential (as is evident, in any case, from an inspection of Fig. 7). Hence, the Devonshire potential is no less reasonable an approximation to it than it was to the original potential  $V_s(\theta, \phi)$ . We have thus reduced the problem, at least in a first approximation, to that of a rotor with a renormalized moment of inertia sitting in a Devonshire potential. It is now straightforward to solve Schrödinger's equation for this system (cf. Appendix C).

### B. Fit to KCl:KCN

In the previous subsection (together with Appendices B and C), we determined the eigenenergies and dipole matrix elements for the levels up to the equivalent of angular quantum number  $J=12$  (limited by the published expansions of the cubic harmonics). In order to apply the model to the full temperature range of our experimental data (1.7–300 K), levels up to about  $J=35$  must be included. However, the reorientational barrier is relatively small (i.e.,  $|K| \ll 2BJ$  for  $J=12$ ) and hence the higher-frequency eigenlevels are well approximated by the eigenfunctions of a free rotor having an appropriately renormalized value for its rotational constant. Therefore, simulated spectra can be generated on a computer by adding together Eq. (C4) for the low-lying levels to Eq. (A8) for levels whose  $J$  values exceed 12. (This implicitly assumes that  $\langle V_{\text{pot}} \rangle_{\theta, \phi} = 0$ , an assumption that is easy to verify for the Devonshire potential.)

There are several free parameters whose values need to be determined in the course of fitting these simulated spectra to the experimental curves: (1) the Devonshire barrier parameter  $K$ , (2) the rotational constants  $B_0^*$  and  $B_1^*$ , and (3) the Lorentzian linewidth (FWHM)  $\gamma$  for each roto-vibrational line. Of these,  $K$  and  $B_0^*$  have the greatest conceptual significance. However, the values for all of these parameters are interdependent in the sense that varying one tends to require adjustments in the values of the others in order to maintain good fits. Ideally, these parameters should be chosen in such a way as to reproduce the following features in the KCl:K<sup>12</sup>C<sup>14</sup>N spectra: (1) the tunnel splitting  $\Delta\nu_{\text{tun}} = 1.05 \pm 0.05 \text{ cm}^{-1}$ , (2) the librational splitting  $\Delta\nu_{\text{lib}} = 11.5 \pm 0.1 \text{ cm}^{-1}$ , (3) the onset of the  $Q$  branch with temperature around 60 K, and (4) the peak-to-peak separations, peak and trough heights, and shapes in the wings of the high-temperature absorption spectra.

The fitting proceeded as follows. We began by assuming that any temperature dependence of  $B_0^*$ ,  $B_1^*$ , and  $K$  could be neglected. In that case, the onset of the  $Q$  branch around 60 K implied a value for  $-K/B_0^*$  equal to  $25 \pm 5$ . This, together with the best possible fit to the tun-

neling spectrum at 1.7 K, meant that  $B_0^* = 0.60 \text{ cm}^{-1}$  and  $K = -15 \text{ cm}^{-1}$ . Next, we noted that varying the value of  $B_1^*$  relative to that of  $B_0^*$  had the effect of changing the  $P$  peak height relative to that of the  $R$  peak. For example, if  $B_1^*$  is smaller in value than  $B_0^*$ , then from Eqs. (A1) and (A3) it follows that the  $P$ -branch transition frequencies will be larger than the corresponding  $R$ -branch frequencies, which will have the effect of decreasing the overlap of adjacent lines in the  $P$  branch and hence of lowering its overall height. This enabled us to find  $B_1^* = 0.592 \text{ cm}^{-1}$ .

Finally, the linewidths were allowed to vary with temperature and with peak position. Figure 3 shows fits to the KCl:K<sup>12</sup>C<sup>14</sup>N spectra at 25, 50, 100, 180, 220, and 300 K. We chose the following simple form for the dependence of the linewidths on peak position: at each temperature, we chose  $\gamma = \gamma_0$  in the trough region and  $\gamma = \gamma_\infty$  in the far wings, and interpolated smoothly (the exact way in which this is done is inconsequential) to find  $\gamma$  between these two extremes. This was found to better fit the data than did a single, frequency-independent linewidth.<sup>37</sup> In particular, one might expect the linewidth to be roughly proportional to the phonon density of states of the host crystal if resonant scattering dominates and if the coupling constants between the phonon bath and the roto-vibrational energy levels of the cyanide defect are the same for all of the levels. In the Debye approximation to the density of states,<sup>38</sup> this would imply that the linewidths should increase quadratically with frequency. In contrast to this, the fitted linewidths, as listed in the caption to the figure, decrease with increasing rotational frequency. This may indicate that phonons couple differently to the low-frequency rotational modes of the cyanide ion than to its high-frequency modes. On the other hand, as far as the temperature variation goes,  $\gamma_0$  and  $\gamma_\infty$  exhibit a roughly quadratic dependence, increasing rapidly with increasing temperature. This temperature dependence is suggestive of homogeneous dephasing processes due to high-temperature phonon scattering.<sup>39</sup>

We can now show that this model reproduces the experimental isotope effect shown in Fig. 2. For this purpose, we generalize Eqs. (10) and (12) to

$$I_v^* = I'_v + c_v = \frac{1}{4}(m_C + m_N)r_v^2 + c_v, \quad (14)$$

$$B_v^* \equiv \frac{\hbar}{8\pi^2 c I_v^*},$$

where the coupling term  $c_v$  is independent of the cyanide mass but would, in general, be expected to depend upon the vibrational excitation  $v$ . (At larger values of  $v$  the average CN bond length  $r_v$  increases, due to the anharmonicity in the vibrational potential, and hence the coupling between the ion and the lattice would almost certainly change.) We found  $r_0$  and  $r_1$  from the values of the free rotational constants  $B_0$  and  $B_1$  and used these, in turn, to obtain  $c_0$  and  $c_1$  from the fitted values of the dressed rotational constants  $B_0^*$  and  $B_1^*$ , for the <sup>12</sup>C<sup>14</sup>N<sup>+</sup> isotope. Finally, values of  $B_0^* = 0.586 \text{ cm}^{-1}$  and  $B_1^* = 0.578 \text{ cm}^{-1}$  for the <sup>13</sup>C<sup>15</sup>N<sup>+</sup> isotope could be calcu-

lated.<sup>40</sup> Notice that these values for the rotational constants of  $^{13}\text{C}^{15}\text{N}^-$  are only 2% smaller than the corresponding values for  $^{12}\text{C}^{14}\text{N}^-$ .

Having determined all of the parameters in the model, computer-simulated spectra could then be generated as a function of temperature for  $^{12}\text{C}^{14}\text{N}^-$  and for  $^{13}\text{C}^{15}\text{N}^-$ . For the sake of simplicity, we assumed that the linewidths  $\gamma_0$  and  $\gamma_\infty$  are identical, at any given temperature, for the two isotopes. Then, Eq. (4) was applied to these modeled spectra at each temperature of interest. In this way, the dashed line in Fig. 2 was obtained in good agreement with the experimental data even though the manifold shape was not reproduced particularly well, as shown by comparing the dashed (calculated) lines with the solid (experimental) lines in Fig. 3.

Finally, we can also discuss the isotopic shift of the tunneling and librational splittings of Fig. 4. The observed  $0.10\text{-cm}^{-1}$  reduction in the tunnel splitting and the  $0.20\text{-cm}^{-1}$  increase in the librational splitting of the heavier isotope can only be reproduced using our model by making the rotational constant  $B_0^*$  of the  $^{13}\text{C}^{15}\text{N}^-$  ion at 1.7 K about 2% smaller than that of the  $^{12}\text{C}^{14}\text{N}^-$  isotope and the barrier parameter  $K$  about 3% larger. This variation in the size of the rotational constant is consistent with the variation calculated above for high temperatures using Eq. (14). Our data is not sufficiently accurate to allow us to determine whether the apparent variation in the size of the barrier height with isotope is a real effect or not.

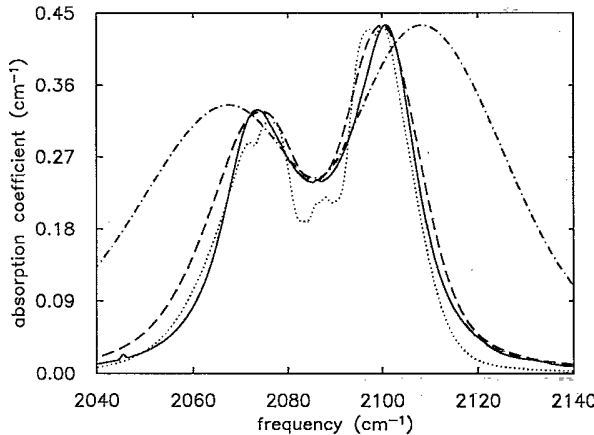


FIG. 8. A comparison of the best fits of the free- and dressed-rotor models to the roto-vibrational spectrum at 140 K. The experimental spectrum is given by the solid curve and is for a KCl:K  $^{12}\text{C}^{14}\text{N}$  0.054-mol % sample plotted previously in Fig. 1(a); the  $\text{Na}^+:\text{CN}^-$  line at  $2080\text{ cm}^{-1}$  and the  $\text{NCO}^-$  line at  $2127\text{ cm}^{-1}$  [compare Fig. 1(a)] have been subtracted out of the spectrum for the sake of clarity. The free-rotor model is given by the dash-dotted curve using  $\gamma_J = \gamma'_J = 15\text{ cm}^{-1}$ . The dashed curve is the fit using our dressed-rotor model with  $B_0^* = 0.60\text{ cm}^{-1}$ ,  $B_1^* = 0.592\text{ cm}^{-1}$ ,  $K = -15\text{ cm}^{-1}$ ,  $\gamma_0 = 14.0\text{ cm}^{-1}$ , and  $\gamma_\infty = 5.4\text{ cm}^{-1}$ . In order to demonstrate the effect of using smaller values for the linewidths, the dotted curve is a plot of the spectrum one obtains using  $\gamma_0 = \gamma_\infty = 2.8\text{ cm}^{-1}$ . Fine structure now appears in the spectrum; a smooth spectrum can only be obtained by using relatively large linewidths.

In Fig. 8, typical results obtained using the free-rotor (dash-dotted curve) and dressed-rotor (dashed curve) models at 140 K are compared to an experimental  $^{12}\text{C}^{14}\text{N}^-$  spectrum (solid curve) from Fig. 1(a). A satisfactory fit of the free-rotor model is not obtained for any choice of the linewidths  $\gamma_J$  and  $\gamma'_J$  in Eq. (A9). In this same figure, the effect of choosing the linewidths  $\gamma_0$  and  $\gamma_\infty$  in the dressed-rotor model to be significantly smaller than the best-fit values is shown (dotted curve). Experimentally unobserved structure begins to be seen near the peaks and in the trough. In general, the range of acceptable values for the linewidths is restricted on the low side by the requirement that no fine structure be seen in the spectra above 10 K and on the high side by the peak-to-peak separations of the experimental spectra. Notice that the resulting fitted linewidths are remarkably large. If these arise from phonon-scattering, absorption, and emission processes, one must conclude that the lifetimes of the rotational levels are very short (on the order of a few psec), in contrast with the long lifetimes<sup>12</sup> of the vibrational levels. This result is consistent with fluorescence measurements: even if only a single roto-vibrational level is excited, the entire manifold is observed to fluoresce, at least on a  $\mu\text{sec}$  time scale.<sup>41</sup>

We next attempt to fit the low-temperature tunneling and librational spectrum (see Fig. 9). The data are given by the asterisks. It is only at this temperature (1.7 K)

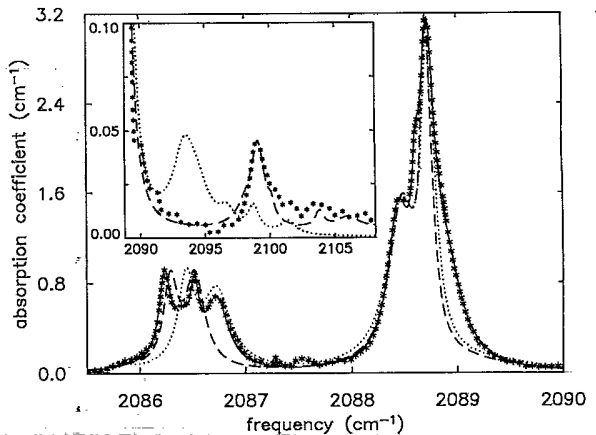


FIG. 9. Fits to the tunneling spectrum and, in the inset, to the librational sideband of KCl:K  $^{12}\text{C}^{14}\text{N}$  0.01 mol % at 1.7 K and  $0.04\text{-cm}^{-1}$  resolution. The experimental data is taken from Fig. 4 and is represented by the asterisks. The dotted curve is a fit using our model with the temperature-independent values  $B_0^* = 0.60\text{ cm}^{-1}$ ,  $B_1^* = 0.592\text{ cm}^{-1}$ , and  $K = -15\text{ cm}^{-1}$ . A better fit is obtained by using  $B_0^* = B_1^* = 0.85\text{ cm}^{-1}$  and  $K = -35\text{ cm}^{-1}$ , as explained in the text, and is plotted as the dashed curve. In this latter case, the parameters for the resulting fit are listed in Table II. The model determines the relative intensities and peak positions of the lines; an overall scaling factor and the widths of the lines were freely chosen so as to give the best possible resemblance to the experimental spectrum. The solid curve is a model-free, computer fit to the experimental tunneling spectrum. Nine Lorentzians were found to be needed in order to obtain a satisfactory fit; the parameters for these Lorentzians are given in Table III.

that sufficient structure was resolved in the spectra to warrant the use of more than two free parameters to describe the linewidths. The dotted curve is the fit obtained using the (temperature-independent) values for the parameters  $B_0^*$ ,  $B_1^*$ , and  $K$  determined above. The matrix elements and the transition frequencies were computed as described in Appendix C; the linewidths were fitted freely for each transition. The fit to the tunneling data is fair, but is by no means perfect.

While the predicted librational sideband (dotted curve in the inset plot in Fig. 9) has the correct shape, it is shifted in frequency in comparison to the experimental spectrum. The only way we can simultaneously reproduce both the experimental librational and tunnel splittings is to increase the values of both  $B_0^*$  and of  $K$ , i.e., we now allow these values to be temperature dependent. (There is no reason at this temperature to allow the value of  $B_1^*$  to be different from that of  $B_0^*$ , so we have chosen them to be equal.) In particular, the dashed curve in Fig. 9 represents the fit obtained when the values  $K = -35 \text{ cm}^{-1}$  and  $B_0^* = 0.85 \text{ cm}^{-1}$  are used. The calculated matrix elements and transition frequencies and the fitted linewidths for this case are listed in Table II. Notice now that the librational sideband is quite well reproduced, in-

cluding its higher-frequency structure, while the fit to the tunneling spectrum is as good as it was before (albeit different).

Clearly, the experimental tunneling spectrum (as given by the asterisks in the main plot in Fig. 9) possesses more lines than are predicted by the Devonshire potential. A detailed fit to the sum and difference tunneling branches (as given by the solid curve in Fig. 9) requires at least nine Lorentzians, whereas the Devonshire model only gives six (namely,  $A_{1g} \leftrightarrow T_{1u}$ ,  $T_{1u} \leftrightarrow T_{2g}$ , and  $T_{2g} \leftrightarrow A_{2u}$ ). The parameters for such a detailed fit are specified in Table III and can be used to quite accurately reproduce the experimental spectrum.

We cannot definitively rule out at present the possibility that some or all of these three "extra" lines may actually be the modes of vibration of cyanide-defect combinations. However, the same number of lines is seen for both isotopes and also for different samples grown under different conditions. Therefore, we suggest that the lines are, in fact, intrinsic to the cyanide-host system. In that case, some suitable perturbation of the Devonshire potential may suffice to explain the observed discrepancies, by partially splitting the remaining degeneracies of the energy levels. The most likely possibility is low-symmetry

TABLE II. Parameters for a fit of the Devonshire model (as given by the dashed line in Fig. 9) to the KCl: $\text{K}^{12}\text{C}^{14}\text{N}$  0.01-mol % tunneling and librational spectrum at 1.7 K. Every transition which makes at least a 1% contribution to the fit has been included. Lorentzians of the form

$$\frac{1}{\pi} \frac{A\gamma/2}{(\nu - \nu_0 - \Delta\nu)^2 + (\gamma/2)^2},$$

where  $\nu_0 = 2087.57 \text{ cm}^{-1}$ , were added together. The positions of the peaks (i.e., the transition frequencies) and the dipole transition matrix elements were calculated as described in Appendix C. The eigenlevels are labeled as  $R^x$ , where  $R$  denotes the representation and  $x$  numbers the levels, in order of increasing energy, for each representation. The amplitude for any given transition is proportional to the product of  $D_{if}$ , the sum of the squares of the matrix elements between the degenerate states of the two eigenlevels in question, and the Boltzmann population factor, with the overall proportionality constant determined by scaling the height of the modeled spectrum to that of the experimental spectrum. The linewidths were allowed to vary freely during the fitting process. The solid line across the middle of the table divides the tunneling transitions from the librational transitions.

Transition $i \rightarrow f$	Peak position $\Delta\nu$ ( $\text{cm}^{-1}$ )	Matrix element squared $D_{if}$	Amplitude $A$ ( $\text{cm}^{-2}$ )	FWHM $\gamma$ ( $\text{cm}^{-1}$ )
$A_{1g}^1 \rightarrow T_{1u}^1$	+0.98	0.964	0.65	0.30
$T_{1u}^1 \rightarrow A_{1g}^1$	-0.98	0.964	0.29	0.22
$T_{1u}^1 \rightarrow T_{2g}^1$	+1.21	1.77	0.52	0.12
$T_{2g}^1 \rightarrow T_{1u}^1$	-1.21	1.77	0.19	0.16
$T_{2g}^1 \rightarrow A_{2u}^1$	+1.66	0.768	0.082	1.0
$A_{2u}^1 \rightarrow T_{2g}^1$	-1.66	0.768	0.020	0.40
$T_{2g}^1 \rightarrow T_{2u}^1$	+10.85	0.343	0.037	2.0
$T_{1u}^1 \rightarrow E_g^1$	+11.61	0.195	0.058	1.1
$A_{2u}^1 \rightarrow T_{2g}^2$	+12.58	0.230	0.0062	0.60
$T_{2g}^1 \rightarrow T_{1u}^2$	+16.30	0.0872	0.0094	0.80
$A_{1g}^1 \rightarrow T_{1u}^2$	+18.49	0.0294	0.020	2.2
$T_{1u}^1 \rightarrow T_{1g}^1$	+22.52	0.0508	0.015	3.0

TABLE III. Parameters for an overall, model-free fit (as given by the solid line in Fig. 9) to the KCl:K  $^{12}\text{C}$   $^{14}\text{N}$  0.01-mol % tunneling spectrum at 1.7 K. The experimental data was found to be well fit by the sum of nine Lorentzians of the form specified in the caption of Table II. The instrumental resolution of  $0.04\text{ cm}^{-1}$  has not been deconvolved from the fitted linewidths.

Peak position $\Delta\nu$ ( $\text{cm}^{-1}$ )	Amplitude $A$ ( $\text{cm}^{-2}$ )	FWHM $\gamma$ ( $\text{cm}^{-1}$ )
-1.62	0.031	0.56
-1.34	0.17	0.14
-1.18	0.10	0.20
-1.05	0.085	0.10
-0.84	0.25	0.26
+0.87	0.45	0.24
+1.04	0.082	0.080
+1.15	0.68	0.17
+1.33	0.41	0.36

distortions arising from internal strain fields in the crystals. Support for this hypothesis was obtained by annealing a low-concentration KCl:KCN sample at  $700^\circ\text{C}$  for 30 h in an inert-gas atmosphere. Some of the lines were observed to shift towards each other in frequency as a result (see Fig. 10). New high-resolution stress-splitting experiments should therefore be helpful in resolving this issue.

The overall fit at 1.7 K (cf. Fig. 9) was improved by selecting the values of the rotational constants and the potential barrier parameter freely, rather than by using the assumed temperature-independent values determined previously. Similarly, we can improve the fit at 25 K by selecting new values for these parameters. We choose (see Fig. 11)  $K = -29\text{ cm}^{-1}$ ,  $B_0^* = 0.70\text{ cm}^{-1}$ , and

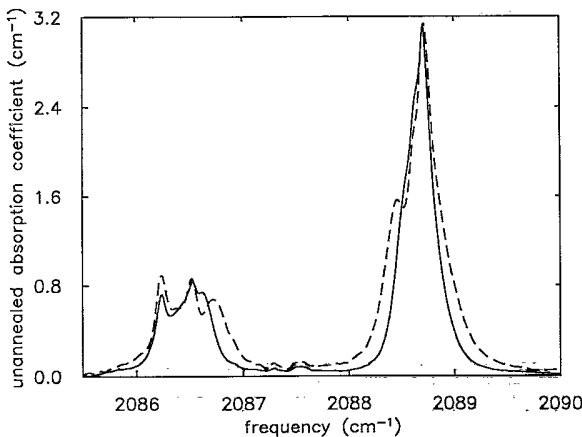


FIG. 10. Effect of annealing a KCl:K  $^{12}\text{C}$   $^{14}\text{N}$  0.01-mol % sample. The dashed curve shows the spectrum for an as-grown sample at 1.7 K, and is the same as the solid curve in the main plot of Fig. 4. The solid curve is the spectrum of a sample which has been annealed at  $700^\circ\text{C}$  for 30 h under helium; it has been scaled vertically so that the peaks of both spectra agree for the purposes of comparison. The spectral resolution was  $0.04\text{ cm}^{-1}$  for both cases.

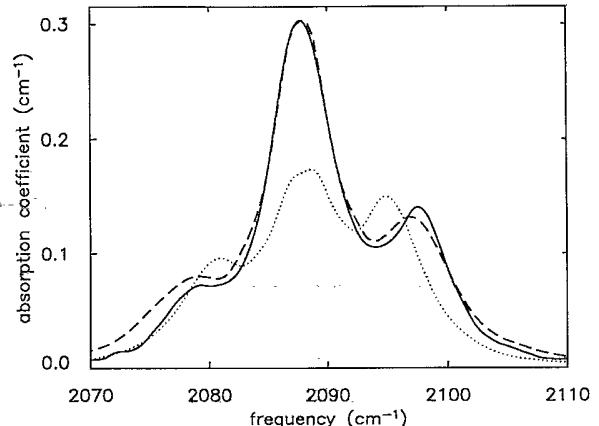


FIG. 11. Improved fit to the KCl:K  $^{12}\text{C}$   $^{14}\text{N}$  0.01-mol % spectrum at 25 K. The experimental data is given by the solid curve and is the same as in Fig. 3. (It has been smoothed slightly in order to reduce the noise.) The dotted curve is the same as the dashed curve in that previous figure, and is the fit obtained using  $B_0^* = 0.60\text{ cm}^{-1}$ ,  $B_1^* = 0.592\text{ cm}^{-1}$ ,  $K = -15\text{ cm}^{-1}$ ,  $\gamma_0 = 2.8\text{ cm}^{-1}$ , and  $\gamma_\infty = 2.8\text{ cm}^{-1}$ . The dashed curve is the fit one obtains using  $B_0^* = 0.70\text{ cm}^{-1}$ ,  $B_1^* = 0.69\text{ cm}^{-1}$ ,  $K = -29\text{ cm}^{-1}$ ,  $\gamma_0 = 1.8\text{ cm}^{-1}$ , and  $\gamma_\infty = 3.4\text{ cm}^{-1}$  instead. These values for  $K$  and  $B_0^*$  are intermediate between those used at higher temperatures (Fig. 3) and those used at 1.7 K (Fig. 9).

$B_1^* = 0.69\text{ cm}^{-1}$ . These values are intermediate between those used for the high-temperature fits in Fig. 3 and those used in the revised fit at 1.7 K in Fig. 9.

### C. Fit to cyanide doped in other hosts

For the other hosts, the data presented in Sec. III C was for RT only. In that case, the crystal-field potentials can be neglected since the barrier heights in all of these hosts are small<sup>16</sup> compared to 300 K. Thus, the model simplifies and the only free parameters are the rotational constants and the linewidths.

The resulting fits are plotted in Fig. 6, giving the values for the parameters  $\nu_0$ ,  $B_0^*$ ,  $B_1^*$ ,  $\gamma_0$ , and  $\gamma_\infty$  listed in Table I. (In general, the value of  $B_1^*$  cannot be found when the  $P$  and  $R$  branches are unresolved from each other; in such cases, for the sake of simplicity, we have used  $B_1^* = B_0^*$ .) Reasonable fits are obtained for all nine hosts. As mentioned earlier, the rotational constants are found to decrease, in general, with increasing host-lattice interionic separation.

Notice that the best fit to the room-temperature KCl:KCN spectrum (cf. Fig. 6) is obtained when a smaller value for  $B_0^*$  is used than the temperature-independent value used previously (in Fig. 3). This continues the trend of the previous subsection, wherein the experimental spectra are found to be best fit if  $B_0^*$  is allowed to decrease with increasing temperature.

From these fitted values of  $B_0^*$ , Eqs. (10) and (12) can be used to deduce experimental values for  $\xi_1$  at RT. These can be compared to the theoretical predictions of Eq. (B7) using the values of the lattice constants  $a$  and of the shape factors ( $\lambda_1 - \lambda_2$ ) listed in Table I. The predict-

ed values turn out to be smaller than the experimentally obtained values by a factor of 3 in every case. In other words, our model correctly reproduces the overall host-dependent trend in the data. But it systematically underestimates the actual magnitude of the contribution of the lattice to the cyanide ion's dressed moment of inertia. Only a small improvement is obtained by including the neighboring halide ions in the model, in addition to the alkali ones.<sup>42</sup> We conclude that the maximum displacements of the neighbors from their mean sites during the dipolar reorientations must be significantly larger than what elastic continuum theory predicts.

## V. DISCUSSION

Our results for KCl:KCN indicate values for the rotational constant  $B_0^*$  which are considerably smaller than the value obtained by Seward and Narayananamurti.<sup>2</sup> The discrepancy originates from the different methods of analysis used. Whereas our values were obtained by globally fitting to the experimental spectra, Seward and Narayananamurti found their value by fitting Eq. (2) to the peak-to-peak separations (i.e., the frequency separations between the *P* and *R* branch absorption peaks) as a function of temperature. In this way, they found  $B=1.25 \text{ cm}^{-1}$  from the slope of a graph of the square of the peak-to-peak separations versus temperature. However, if our experimental data is plotted on such a graph, we find, in contrast to Seward and Narayananamurti's results, that the data points are noncollinear and a best-fit line does not go through the origin.

Wilk and Lüty, in a recent paper,<sup>16</sup> have tried to improve Seward and Narayananamurti's approach by calculating a correction term (in  $T^{3/2}$ ) to Eq. (2), obtained by including the higher-order  $D$  rotational constant in the derivation. Using this method with our experimental data, we find  $B=1.30 \text{ cm}^{-1}$  and  $D=3.1 \times 10^{-3} \text{ cm}^{-1}$ , which not only again gives too large of a value for  $B$ , as determined by our numerical simulations of the roto-vibrational manifold, but also gives much too large of a value for  $D$  [compare Eq. (A6); if anything,  $D$  might be expected to decrease in value due to the lattice dressing, as compared to its free value]. The *P*- and *R*-branch peaks begin to distort in shape if such a large value for  $D$  is used in the simulations. Just to see, however, whether any other values for  $D_0^*$ , and even  $D_1^*$  (i.e., allowing different values for  $D$  in the ground and excited vibrational states), might improve the fits, we have repeated our fitting procedure with  $D_0^*$  and  $D_1^*$  as additional (temperature-independent) free parameters, but we did not find that the resulting fits were significantly better than the previous fits in which we had used  $D_0^*=D_1^*=0$ .

In actuality, Eq. (2), or any simple correction to it, cannot be used to analyze the experimental data because it was derived with the implicit assumptions that the orientational potential and the roto-vibrational linewidths are negligible. Furthermore, even for our best fits, the peak-to-peak separations were not all that accurately reproduced; in our opinion, attempting to extract the values of physically meaningful parameters from the peak-to-peak separations alone (or from any other single "local" feature) is intrinsically unreliable. In this paper, we have

emphasized that global fitting and comparison techniques are to be preferred, owing to the complexity of the actual details of the system, as reflected by our inability to fit the spectral shapes in detail.

We conclude that the rotational constants for KCl:KCN are even smaller than the values reported in previous ir investigations.<sup>43</sup> The coupling between the cyanide defect and the potassium chloride host lattice is therefore even stronger than was previously believed. A measure of this strength is given by the magnitude of the coupling coefficient  $\xi_1$ , which physically represents the maximum displacement of a nearest-neighboring potassium ion from its average position due to the reorienting cyanide ion.

It appears from the present study that both the rotational constant  $B_0^*$  and the barrier parameter  $K$  are temperature dependent,<sup>44</sup> their absolute values decreasing with increasing temperature. Consider first the temperature dependence of the potential barrier. In KCl, the cyanide ions fit rather snugly into the lattice and it is conceivable that the thermal expansion and random ionic motion of the matrix with increasing temperature will produce a significant decrease in the size of the reorientational barriers. Support for this idea comes from a result by Field and Sherman.<sup>30</sup> They found that a *Q* branch appears in the KCl:KCN spectrum at 90 K when 10–20 kbar of hydrostatic pressure is applied to the sample. But such pressures only produce small changes in the lattice constants, on the order of 1–2 %, comparable to the thermal contraction upon cooling from RT to low temperatures.<sup>45</sup> Evidently, the cyanide ions are very sensitive to even slight changes in their local environment.

Next, with regards to the temperature dependence of the rotational constant, the best-fit values for KCl:KCN decrease by roughly a factor of 2 from 1.7 to 300 K, despite the thermal expansion of the host lattice. In fact, our theory actually predicts a slight *increase* in the value of  $B_0^*$  with increasing temperature [compare Eqs. (10) and (11)], owing to a stronger average coupling between  $\langle 111 \rangle$  oriented defects and the lattice, as compared to randomly oriented ones. Similarly,  $B_0^*$  decreases, in general, with increasing lattice interionic spacing for cyanide doped into a number of different alkali halide hosts (cf. Table I). Naively, however, one might have expected the ions to become more nearly free as the cavities in which they are located increase in size. A few possible explanations for this seemingly anomalous result can be proposed.

First of all, the cyanide ions might move off center, as the cavity size increases, which could result in an increase in the moment of inertia of the dipoles, in analogy with the term given by Eq. (6). One direct means of observing such an effect is obtained from measurements of the electric dipole moment. As the charged impurity moves off center, the effective dipole moment of the system would, in general, increase. As far as the potassium salts are concerned, however, the size of the lattice-substituted dipole moment is too small to be consistent with any substantial displacement of the c.m. and furthermore, no variation of the dipole moment with host is observed.<sup>46</sup> Hence, this explanation seems very unlikely.

A second possibility is that when the surrounding alkali ions are located farther away from a given cyanide ion, they have more room in which to move so that their displacements from equilibrium during the reorientations of the cyanide ion might be larger. In such a case, it follows from Eqs. (8) and (10) or (11) that this would give rise to a larger effective moment of inertia and hence to a smaller value for the rotational constant. From the point of view of our model, this would arise as a change in the magnitude of the elastic dipole moment of the matrix-substituted ion and hence in the value of  $\xi_1$  in Eq. (B7). In fact, for the three hosts (KCl, KBr, and KI) in Table I for which  $(\lambda_1 - \lambda_2)$  has been measured, this value does vary from host to host, in just such a manner that the theoretical values for  $B_0^*$  decrease with increasing lattice constant. So, this explanation has some credibility.

Thirdly, an overall decrease in the values of  $B_0^*$  for the rubidium hosts, as compared to the corresponding potassium hosts, is expected simply because a rubidium is much heavier than a potassium ion. The dressing correction to the moment of inertia of a cyanide ion is proportional to the alkali ion mass [cf. Eqs. (10) or (11)]. Indeed, we calculate theoretical values for  $B_0^*$  which are smaller for the rubidium hosts than for the corresponding potassium hosts. Similarly, by including the next-neighbor halide ions in the model, we predict that  $B_0^*$  should decrease with increasing halide ion mass, for any given alkali host series, as is observed.<sup>42</sup>

In Table IV, we have summarized the fitted values for KCl:K<sup>12</sup>C<sup>14</sup>N for the five parameters in our model at the temperatures investigated in this study. The corresponding fits were previously plotted as the dashed curves in the following figures: 1.7 K, Fig. 9; 25 K, Fig. 11; 50, 100, 180, and 220 K, Fig. 3; 140 K, Fig. 8; and finally, RT, Fig. 6. Even with this many free parameters at our disposal, the simulations are in noticeable disagreement with the experimental spectra. We therefore conclude that other physical ideas may need to be introduced in order to improve the agreement between theory and experiment.

## VI. SUMMARY

The key aspects of the present paper can be summarized as follows.

(1) The isotopic dependence of the KCl:K<sup>12</sup>C<sup>14</sup>N and KCl:K<sup>13</sup>C<sup>15</sup>N spectra above 100 K, as quantified by an integrated ratio of the manifold widths for the two isotopes at each temperature, are not consistent with a free-rotor model.

(2) A dressed-rotor model has been developed, in which elastic deformations of the host-lattice atoms surrounding a given rotating cyanide ion are permitted to relax adiabatically, leading to an enhanced value of the moment of inertia of the dipole. Assuming that the values of  $K$ ,  $\gamma_0$ , and  $\gamma_\infty$  are the same for both isotopes, and using our theory to compute  $B_0^*$  and  $B_1^*$  for KCl:K<sup>13</sup>C<sup>15</sup>N, the measured isotope effect is consistent with this model.

(3) The model involves five free parameters—the rotational constants  $B_0^*$  and  $B_1^*$ , the Devonshire potential barrier parameter  $K$ , and the linewidths  $\gamma_0$  and  $\gamma_\infty$ —all of which are found to be temperature dependent; their fitted values for the case of KCl:K<sup>12</sup>C<sup>14</sup>N are listed in Table IV. Surprisingly, the fits are not in detailed agreement with the experimental spectra.

(4) The fitted values of the rotational constants for KCl:KCN decrease with increasing temperature, despite the thermal expansion of the host; similarly, the rotational constants tend to decrease, on average, with increasing lattice interionic separation for CN<sup>-</sup> in the nine hosts studied.

(5) An explicit calculation of  $B_0^*$  for cyanide doped into the six potassium and rubidium salts investigated here results in values which are about three or four times larger than the experimentally fitted values; however, the overall trend that  $B_0^*$  decreases from a maximum value for KCl down to a minimum value for RbI is correctly reproduced.

(6) The potential barrier parameter  $K$  decreases with increasing temperature, as might be expected.

(7) The quadratic temperature dependence of the

TABLE IV. Summary of the best-fit values for the parameters in our dressed-rotor model for KCl:K<sup>12</sup>C<sup>14</sup>N at various temperatures  $T$ . The five parameters are the rotational constants  $B_0^*$  and  $B_1^*$  in the ground and first excited vibrational levels, respectively, the Devonshire potential barrier parameter  $K$ , and the linewidths (FWHM) of the roto-vibrational lines near the manifold center ( $\gamma_0$ ) and at high rotational frequencies in the wings of the spectra ( $\gamma_\infty$ ). The notation “NA” means that the value of the parameter at that particular temperature is either not well defined or could not be determined from the experimental data.

$T$ (K)	$B_0^*$ (cm <sup>-1</sup> )	$B_1^*$ (cm <sup>-1</sup> )	$K$ (cm <sup>-1</sup> )	$\gamma_0$ (cm <sup>-1</sup> )	$\gamma_\infty$ (cm <sup>-1</sup> )
1.7	0.85	NA	-35	NA	NA
25	0.70	0.690	-29	1.8	3.4
50	0.60	0.592	-15	4.4	3.4
100	0.60	0.592	-15	8.8	4.4
140	0.60	0.592	-15	14.0	5.4
180	0.60	0.592	-15	18.0	8.0
220	0.60	0.592	-15	24.0	10.0
297.1	0.47	0.463	NA	36.0	12.0

linewidths suggests that phonon dephasing is the source of the broadening above 25 K; however, the fitted linewidths are found to decrease with increasing transition frequency, contrary to what one might expect on the basis of the frequency dependence of the phonon density of states.

(8) At 1.7 K, new structure was identified in the tunneling spectra of KCl:KCN; introducing dislocations into the sample destroyed this tunnel splitting. Not all of the observed lines can be explained using the Devonshire model.

(9) An isotopic dependence is found for the values of both  $K$  and  $B_0^*$  for KCl:KCN at 1.7 K. The variation of  $B_0^*$  is consistent with the dressed-rotor model.

In conclusion, our semiclassical description of the cyanide-defect-host-lattice coupling has been shown to be reasonably successful in explaining many of the experimental observations in a quantitative manner. This approach may also find applications in the study of other matrix-isolated ionic defect systems. An example is CsCl:OH<sup>-</sup> which, like KCl:CN<sup>-</sup>, has a double-humped roto-vibrational spectrum.<sup>47</sup>

#### ACKNOWLEDGMENTS

C. E. Mungan would like to thank G. Schmidt for instruction in the growth of doped alkali halide crystals. We acknowledge W. P. Ambrose and S. P. Love for numerous discussions of various theoretical and experimental details; correspondence with E. R. Grannan has also been helpful. We would like to thank R. H. Silsbee for critically reading the manuscript and making many valuable suggestions. This work has been supported by National Science Foundation Grant No. NSF-DMR-88-18558 from Cornell University's Material Science Center; C. E. Mungan, R. C. Spitzer, and A. J. Sievers acknowledge additional support from U.S. Army Research Office Contract No. ARO-DAAL03-89-K-0053.

#### APPENDIX A: THE FREE-ROTOR MODEL FOR CYANIDE

When CN<sup>-</sup> is doped into an alkali halide, it substitutes for the halide ions in the lattice. If we assume that the centers of mass of the ellipsoidal cyanide ions are fixed in position at the lattice sites, then each dipole will be restricted to three degrees of freedom: one vibrational and two angular. Next, it is conventional to assume that the sole effect of the surrounding lattice is to set up an octahedral potential field (which physically arises from the electromagnetic and quantum-mechanical repulsive forces existing between the salt ions and the cyanide ion) in the two angular coordinates. However, in at least some of the alkali halides, these reorientational potentials are weak enough that, at room temperature, say, the cyanide ions possess an average thermal energy well in excess of the barrier heights. In that case, the perturbing influence of the potential upon the rotational motion of the dipoles is negligible and the cyanide ions become free rotors. Consequently, the rotational quantum number  $J$  becomes well defined and the well-known rotational-vibrational spectrum is obtained.

In absorption, the infrared dipole selection rules are  $\Delta v = +1$  (where  $v$  is the stretching vibrational quantum number) and  $\Delta J = \pm 1$ , giving rise to two sequences of spectral lines:  $\Delta J = +1$ , known as the  $R$  branch, and  $\Delta J = -1$ , known as the  $P$  branch. Referring to Herzberg,<sup>11</sup> the transition frequencies of the vibrating rotor can be shown to be

$$\nu(v_f, J_f; v_i, J_i) \equiv \frac{E_f - E_i}{hc} = G(v_f) - G(v_i) + F_{v_f}(J_f) - F_{v_i}(J_i), \quad (\text{A1})$$

where  $i$  and  $f$  refer to the initial and final states, respectively. The term values  $G(v)$  of the vibrating anharmonic oscillator are given by

$$G(v) \approx \nu_e(v + \frac{1}{2}) - \nu_e x_e(v + \frac{1}{2})^2, \quad (\text{A2})$$

where the second term is the lowest-order anharmonic correction. Measurement of the center frequency  $\nu_0$  of the fundamental spectrum (the  $v = 0 \rightarrow 1$  transition) and that of the first overtone ( $v = 0 \rightarrow 2$ ) enables one to calculate  $\nu_e$  and  $x_e$ . These center frequencies, however, cannot, in general, be accurately determined simply from a visual inspection of the relevant spectra. On the contrary, these values must be determined by fitting to the spectra, according to the procedure described in Sec. IV. The resulting values for the parameters  $\nu_0$ ,  $\nu_e$ , and  $x_e$  in the case of KCl:KCN are given in Table V.

The dependence of the transition frequencies upon  $J \equiv J_i$  (with  $J_f = J_i \pm 1$ ) is determined by the term values of the vibrating anharmonic rotor:

$$F_v(J) \approx B_v J(J+1) - D_0 J^2(J+1)^2, \quad (\text{A3})$$

where

$$B_v \approx B_0 - \alpha_e v \quad (\text{A4})$$

with  $\alpha_e \ll B_0$  (where the signs have been chosen so that all quantities are positive).  $B_v$  and  $D_0$  are the rotational constants of the CN<sup>-</sup> ion. They represent the rotational contribution to the energy of the ion. It is straightforward to show that

$$B_0 = \frac{\hbar}{8\pi^2 c I_0}, \quad (\text{A5})$$

where  $I_0$  is the moment of inertia of the ion in its ground vibrational state. The value for this latter quantity is  $\mu r_0^2$ , where  $\mu \equiv m_C m_N / (m_C + m_N)$  is the reduced mass of the dipole and  $r_0$  is the average internuclear separation of the ion in its ground vibrational state. The term in  $D_0$  is the lowest-order correction to the spectrum when the vibrations of the ion are coupled to its rotations. This correction term can easily be derived semiclassically by considering a model of two point masses attached by a spring and determining by how much the spring stretches when the ion rotates. In this way, one finds

$$D_0 = \frac{4B_0^3}{\nu_0^2}, \quad (\text{A6})$$

TABLE V. Parameters for the free-rotor model for matrix-isolated cyanide. The value tabulated for  $r_0$ , the average internuclear separation of the ion in its ground vibrational state, is that obtained from neutron-diffraction measurements [N. Elliott and J. Hastings, *Acta Crystallogr.* **14**, 1018 (1961)] in pure KCN [which disagrees somewhat with the value 1.05 Å obtained by x-ray diffraction (Ref. 31)]. Note that negligible error is made in assuming that the CN bond length  $r_0$  has the same value in KCl:KCN (for any CN<sup>-</sup> isotope), say, even at very low dopant concentrations, as it does in pure KCN, because even slight changes in the bond length produce significant variations (Ref. 30) in the stretching mode frequency  $\nu_0$ . The values of the parameters  $\nu_e$ ,  $x_e$ , and  $\nu_0$  are for a temperature of 1.7 K (the former two of which are extrapolated values from RT measurements). The rotational constants  $B_0$ ,  $\alpha_e$ , and  $D_0$  were computed using all of the above parameters, as explained in the text.

Parameter	Isotope	Value
$r_0$		1.16 Å
$\nu_e$	KCl: <sup>12</sup> C <sup>14</sup> N <sup>-</sup>	2115 cm <sup>-1</sup>
	KCl: <sup>13</sup> C <sup>15</sup> N <sup>-</sup>	2041 cm <sup>-1</sup>
$x_e$	KCl: <sup>12</sup> C <sup>14</sup> N <sup>-</sup>	$6.4 \times 10^{-3}$
	KCl: <sup>13</sup> C <sup>15</sup> N <sup>-</sup>	$6.5 \times 10^{-3}$
$\nu_0$	KCl: <sup>12</sup> C <sup>14</sup> N <sup>-</sup>	2087.57 cm <sup>-1</sup>
	KCl: <sup>13</sup> C <sup>15</sup> N <sup>-</sup>	2011.61 cm <sup>-1</sup>
$B_0$	<sup>12</sup> C <sup>14</sup> N <sup>-</sup>	1.94 cm <sup>-1</sup>
	<sup>13</sup> C <sup>15</sup> N <sup>-</sup>	1.80 cm <sup>-1</sup>
$\alpha_e$	<sup>12</sup> C <sup>14</sup> N <sup>-</sup>	0.017 cm <sup>-1</sup>
	<sup>13</sup> C <sup>15</sup> N <sup>-</sup>	0.016 cm <sup>-1</sup>
$D_0$	<sup>12</sup> C <sup>14</sup> N <sup>-</sup>	$6.7 \times 10^{-6}$ cm <sup>-1</sup>
	<sup>13</sup> C <sup>15</sup> N <sup>-</sup>	$5.8 \times 10^{-6}$ cm <sup>-1</sup>

which agrees with the quantum-mechanical result. The correction term in  $\alpha_e$  arises due to the anharmonicity of the vibrational potential, so that the rotational constants vary slightly from one vibrational level to another. Using a Morse potential to model this anharmonicity, for example, one finds

$$\alpha_e \cong \frac{6B_0^2}{\nu_e} \sqrt{(x_e \nu_e)/B_0 - 1} . \quad (\text{A7})$$

In Table V, we have listed the calculated values for  $B_0$ ,  $\alpha_e$ , and  $D_0$  using published values for the atomic masses and the cyanide bond length together with the measured values of  $\nu_0$ ,  $x_e$ , and  $\nu_e$ . It turns out that the values of  $D_0$  are far too small to have any observable effect upon the spectra and so we can neglect them (by setting them equal to zero).

Now, the spectral line shape (i.e., the absorption as a function of frequency) in this free-rotor model is

$$\alpha(\nu) \propto \sum_{J=0}^{\infty} \nu_{J+1,J} (J+1) e^{-F_0(J)hc/kT} f_J(\nu' - \nu_{J+1,J}) + \sum_{J=1}^{\infty} \nu_{J-1,J} J e^{-F_0(J)hc/kT} f'_J(\nu' - \nu_{J-1,J}) , \quad (\text{A8})$$

where the first sum is over the roto-vibrational lines in the  $R$  branch and the second sum runs over the lines in the  $P$  branch. The constant of proportionality can, in principle, be explicitly calculated for a given system at a given temperature but is more simply handled by treating it as an unknown overall scaling factor to be determined experimentally. In the above expression, the functions  $f_J(\nu)$  and  $f'_J(\nu)$  specify the line shapes of the individual roto-vibrational lines. In particular, it can reasonably be assumed that the lines have a Lorentzian line shape

$$f_J(\nu) = \frac{1}{\pi} \frac{\gamma_J/2}{\nu^2 + (\gamma_J/2)^2} \quad \text{and} \quad (\text{A9})$$

$$f'_J(\nu) = \frac{1}{\pi} \frac{\gamma'_J/2}{\nu^2 + (\gamma'_J/2)^2} ,$$

with linewidths (FWHM)  $\gamma_J$  and  $\gamma'_J$  to be determined by fitting to the experimental data.

## APPENDIX B: ELASTIC DEFECT-HOST INTERACTION TERM

We use classical elasticity theory to derive the form of the coupling coefficients  $\xi_1$  and  $\xi_2$  and to provide a rough estimate of their numerical values. The problem can be solved analytically only for the case of an isotropic host medium. In that case, there are only two independent elastic constants,<sup>48</sup>

$$c_{ijkl} = \lambda \delta_{ij} \delta_{kl} + \mu (\delta_{ik} \delta_{jl} + \delta_{il} \delta_{jk}) , \quad (\text{B1})$$

where  $\lambda$  is called the Lamé coefficient and  $\mu$  is the shear modulus. The displacement field  $\mathbf{u}$  of the medium at  $\mathbf{r} = (x, y, z)$  (with respect to the crystal axes) due to an elastic dipole at the origin is<sup>49</sup>

$$u_i(\mathbf{r}) = - \sum_{j,k=1}^3 Q_{jk} \frac{\partial}{\partial r_k} u_{ij}(\mathbf{r}) , \quad (\text{B2})$$

where the Green's function for the displacement field is<sup>50</sup>

$$u_{ij}(\mathbf{r}) = \frac{1}{8\pi\mu r} \left[ 2\delta_{ij} + \left( \frac{\lambda+\mu}{\lambda+2\mu} \right) \left[ \frac{r_i \cdot r_j}{r} - \delta_{ij} \right] \right] \quad (\text{B3})$$

and where the elastic dipole tensor is<sup>51</sup>

$$Q_{jk} = 2(\lambda_1 - \lambda_2) V_0 \mu (\alpha_j \alpha_k - \frac{1}{3} \delta_{jk}) . \quad (\text{B4})$$

Here  $\alpha_i$  is the direction cosine between the symmetry axis of the elastic dipole (i.e., the major axis of the ellipsoid) and the  $i$ th crystal axis,  $(\lambda_1 - \lambda_2)$  is the so-called shape factor<sup>52</sup> of the defect, and  $V_0 = a^3/4$  is the volume of a primitive unit cell in the host lattice.

Inserting Eqs. (B3) and (B4) into (B2), denoting the orientation of the CN<sup>-</sup> ion by  $\beta_1$  (with respect to the  $+z$  axis, and considering, for example, the displacement of the potassium ion sitting at  $(a/2, 0, 0)$ , we obtain

$$u_x = \frac{(\lambda_1 - \lambda_2)a}{8\pi} \left[ \frac{3\lambda + 5\mu}{\lambda + 2\mu} \right] [\cos(2\beta_1) + \frac{1}{3}] . \quad (\text{B5})$$

Comparing this with Eq. (8), the elastic displacements of the nearest neighbors, we obtain the coupling coefficients

$$\xi_1 = \frac{(\lambda_1 - \lambda_2)a}{8\pi} \left[ \frac{3\lambda + 5\mu}{\lambda + 2\mu} \right], \quad \xi_2 = \frac{1}{3}\xi_1. \quad (\text{B6})$$

In order to evaluate these terms numerically, we average over the actual anisotropic elastic constants<sup>53</sup>  $c_{11} = 3.98 \times 10^{10}$  Pa,  $c_{12} = 0.62 \times 10^{10}$  Pa, and  $c_{44} = 0.625 \times 10^{10}$  Pa, to obtain  $\lambda$  and  $\mu$ . The procedure is described in Chap. 13 of Hirth and Lothe<sup>48</sup> and one obtains<sup>54</sup>  $\mu = 1.047 \times 10^{10}$  Pa and  $\lambda = 1.042 \times 10^{10}$  Pa, or, in other words,  $\mu \approx \lambda$ , so that

$$(3\lambda + 5\mu)/(\lambda + 2\mu) \approx \frac{8}{3},$$

and thus,

$$\xi_1 = \frac{(\lambda_1 - \lambda_2)a}{3\pi}. \quad (\text{B7})$$

The shape factor  $(\lambda_1 - \lambda_2)$  was determined by Beyeler<sup>55</sup> to be equal to 0.18 from low-temperature uniaxial  $\langle 110 \rangle$  stress-splitting measurements. One thus obtains  $\xi_1 = 0.12$  Å, the maximum displacement of the neighboring potassium ions from their mean positions due to the elastic interaction. This value must only be considered to be a crude estimate of the actual value, however, for the simple reason that, near to the defect, one cannot expect the crystal to be well approximated as a continuous, isotropic, elastic medium. Note, however, that  $\xi_1$  does not depend (explicitly) on the elastic constants,<sup>56</sup> so that refining the calculations for  $\mu$  and  $\lambda$  near the defect would not be expected to change the value of  $\xi_1$  very much.

### APPENDIX C: THE DEVONSHIRE MODEL

We use the Rayleigh-Ritz variational method to find the low-lying levels following the procedure described by Sauer.<sup>57</sup> Briefly, Schrödinger's equation with the Devonshire potential and a renormalized rotational constant  $B^*$  is

$$-B^* \nabla^2 |\psi_{nR}\rangle - K [P_4^0(\cos\theta) + \frac{1}{168} P_4^4(\cos\theta)\cos(4\phi)] |\psi_{nR}\rangle = E_{nR} |\psi_{nR}\rangle \quad (\text{C1})$$

for the  $n$ th wave function  $\psi_{nR}$  of representation  $R$  of the  $O_h$  point group ( $R = A_{1g}, A_{1u}, A_{2g}, A_{2u}, E_g, E_u, T_{1g}, T_{1u}, T_{2g}, T_{2u}$ ) having energy eigenvalue  $E_{nR}$ . The wave functions are written as a linear combination of the orthonormalized cubic harmonics:

$$|\psi_{nR}\rangle = \sum_{J,i,t} a_{Jit}^{nR} |\chi_{Jit}\rangle, \quad (\text{C2})$$

where  $J$  denotes the angular quantum number,  $t$  denotes the component ( $t_{\max} = 1$  for  $A$  representations, 2 for  $E$  representations, and 3 for  $T$  representations), and  $i$  is an index for the cases where several harmonics of equal  $J$  and  $t$  belong to the same representation  $R$ . The cubic harmonics, in turn, are expanded in terms of spherical harmonics up to  $J=12$  by Altmann and Cracknell.<sup>58</sup>

$$|\chi_{Jit}\rangle = \sum_m b_m^{Jit} |Y_{Jm}\rangle. \quad (\text{C3})$$

Hence, the expansion coefficients  $a_{Jit}^{nR}$  and the energy eigenvalues  $E_{nR}$  are found by numerically solving a secular equation for each of the ten representations. For this purpose, we have computed the components of each matrix analytically, using the expansion formulas for  $P_4^0(\cos\theta)Y_{Jm}$  and  $P_4^4(\cos\theta)\cos(4\phi)Y_{Jm}$  in terms of spherical harmonics given in Devonshire's paper.<sup>21</sup> Finally, the squares of the dipole transition matrix elements

$$3|\langle \psi_{n'R} | \cos\theta | \psi_{nR} \rangle|^2$$

were evaluated, using the expressions for the dipole transition matrix elements between the free-rotor states (i.e., the spherical harmonics) given by Sommerfeld.<sup>59</sup> These matrix elements were, in turn, summed over the degenerate initial and final states for a total of 903 dipole-allowed nondegenerate transitions between eigenlevels. We denote the eigenlevels by  $R^x$ , where  $x$  numbers the levels for any given representation  $R$  in order of increasing energy; we denote the summed squares of the matrix elements between eigenlevels  $i$  and  $f$  as  $D_{if} = D_{fi}$ .

The resulting spectral absorption line shape is then given by

$$\alpha(\nu') \propto \sum_{i,f} [\nu_{fi}^R D_{fi} e^{-E_{0i}/k} {}^T f_{fi} (\nu' - \nu_{fi}^R) + \nu_{if}^P D_{if} e^{-E_{0f}/k} {}^T f_{if} (\nu' - \nu_{if}^P)] \quad (\text{C4})$$

[compare Eq. (A8)], where the transition frequencies are

$$\nu_{fi}^R \equiv \nu_0 + (E_{1f} - E_{0i})/h \quad (\text{C5a})$$

for the  $R$  branch, and

$$\nu_{if}^P \equiv \nu_0 + (E_{1i} - E_{0f})/h \quad (\text{C5b})$$

for the  $P$  branch. [We use the notation  $E_{vi}$  to indicate the energy of the  $i$ th level in the Devonshire model solved using  $B^* = B_v^*$  in Eq. (C1).]

\*Present address: Lockheed Palo Alto Research Laboratory, 3251 Hanover Street, Palo Alto, CA 94304.

<sup>1</sup>W. F. Sherman and G. R. Wilkinson, in *Vibrational Spectroscopy of Trapped Species*, edited by H. E. Hallam (Wiley, New York, 1973), pp. 245–354.

<sup>2</sup>W. D. Seward and V. Narayananamurti, Phys. Rev. **148**, 463

(1966).

<sup>3</sup>R. Callender and P. S. Pershan, Phys. Rev. A **2**, 672 (1970).

<sup>4</sup>R. W. Dreyfus, Phys. Rev. **188**, 1340 (1969).

<sup>5</sup>D. Walton, H. A. Mook, and R. M. Nicklow, Phys. Rev. Lett. **33**, 412 (1974).

<sup>6</sup>A. Diaz-Gongora and F. Lüty, Phys. Status Solidi B **86**, 127

- (1978).
- <sup>7</sup>R. C. Spitzer, W. P. Ambrose, and A. J. Sievers, Phys. Rev. B **34**, 7307 (1986).
- <sup>8</sup>A. T. Fiory, Phys. Rev. B **4**, 614 (1971).
- <sup>9</sup>N. E. Byer and H. S. Sack, Phys. Status Solidi **30**, 569 (1968); **30**, 579 (1968).
- <sup>10</sup>R. Windheim, Solid State Commun. **18**, 1183 (1976).
- <sup>11</sup>G. Herzberg, *Molecular Spectra and Molecular Structure I: Spectra of Diatomic Molecules*, 2nd ed. (Van Nostrand, New York, 1950), Chap. III, pp. 66–145.
- <sup>12</sup>Y. Yang and F. Lüty, Phys. Rev. Lett. **51**, 419 (1983).
- <sup>13</sup>T. R. Gosnell, R. W. Tkach, and A. J. Sievers, Solid State Commun. **53**, 419 (1985).
- <sup>14</sup>R. W. Tkach, T. R. Gosnell, and A. J. Sievers, Opt. Lett. **9**, 122 (1984); T. R. Gosnell, A. J. Sievers, and C. R. Pollock, *ibid.* **10**, 125 (1985).
- <sup>15</sup>D. M. Kammen, T. R. Gosnell, R. W. Tkach, and A. J. Sievers, J. Chem. Phys. **87**, 4371 (1987); W. E. Moerner, A. R. Chraplyvy, and A. J. Sievers, Phys. Rev. B **29**, 6694 (1984); F. Lüty, Cryst. Lattice Defects Amorphous Mater. **12**, 343 (1985).
- <sup>16</sup>S. R. Wilk and F. Lüty, Phys. Status Solidi B **146**, 303 (1988).
- <sup>17</sup>H. B. Shore, Phys. Rev. Lett. **17**, 1142 (1966); L. M. Sander and H. B. Shore, Phys. Rev. B **3**, 1472 (1971); H. B. Shore and L. M. Sander, *ibid.* **6**, 1551 (1972); **12**, 1546 (1975).
- <sup>18</sup>R. Pirc and P. Gosar, Phys. Kondens. Mater. **9**, 377 (1969).
- <sup>19</sup>V. Narayananmurti and R. O. Pohl, Rev. Mod. Phys. **42**, 201 (1970).
- <sup>20</sup>F. Bridges, CRC Crit. Rev. Solid State Sci. **5**, 1 (1975).
- <sup>21</sup>A. F. Devonshire, Proc. R. Soc. London, Ser. A **153**, 601 (1936).
- <sup>22</sup>H. C. Allen, Jr., E. D. Tidwell, and E. K. Plyler, J. Chem. Phys. **25**, 302 (1956).
- <sup>23</sup>H. W. Morgan and P. A. Staats, J. Appl. Phys. **33**, 364 (1962); I. C. Hisatsune and N. H. Suarez, Inorg. Chem. **3**, 168 (1964).
- <sup>24</sup>V. Schettino and I. C. Hisatsune, J. Chem. Phys. **52**, 9 (1970); M. A. Cundill and W. F. Sherman, Phys. Rev. **168**, 1007 (1968).
- <sup>25</sup>Two main pieces of evidence support this hypothesis. First, a systematic investigation of the integrated strength of this peak with cyanide concentration [e.g., compare the dashed curve in Fig. 1(b) at 0.39% concentration and 100 K to the uppermost solid curve which is for 0.052% concentration and the same temperature] shows a quadratic dependence. Secondly, the peak position is 0.9 cm<sup>-1</sup> lower in frequency than our fitted value for  $\nu_0$ , consistent with the results of Grant and Klein [M. B. Grant and M. V. Klein, Phys. Rev. B **32**, 1212 (1985)], if their data is extrapolated down to lower concentrations. We do not presently have explanations for the fact that this pair peak is visible only in the case of the <sup>13</sup>C<sup>15</sup>N<sup>-</sup> isotope, nor for why it persists to high temperatures (in the case of the 0.39-mol % sample, the peak remains visible at RT), where thermal reorientation energies might have been expected to overwhelm the energy of interaction between two neighboring cyanide ions.
- <sup>26</sup>A. S. Barker, Jr. and A. J. Sievers, Rev. Mod. Phys. **47** Suppl. 2, S1 (1975).
- <sup>27</sup>R. M. Hexter and D. A. Dows, J. Chem. Phys. **25**, 504 (1956).
- <sup>28</sup>M. Gomez, S. P. Bowen, and J. A. Krumhansl, Phys. Rev. **153**, 1009 (1967).
- <sup>29</sup>In passing, we mention that the room-temperature spectrum of the sample was unaltered by the introduction of the dislocations.
- <sup>30</sup>G. R. Field and W. F. Sherman, J. Chem. Phys. **47**, 2378 (1967).
- <sup>31</sup>J. M. Bijvoet and J. A. Lely, Rec. Trav. Chim. Pays-Bas **59**, 908 (1940).
- <sup>32</sup>A rough numerical estimate of the size of the electric coupling term can be obtained by expanding, to first order in displacements  $q_i$  of the neighboring potassium ions, the energy of interaction between the local dipole moment (i.e., using the Lorentz local-field correction, cf. Ref. 8) of the CN<sup>-</sup> ion and the fields set up by the neighboring K<sup>+</sup> ions. In this way, it can be estimated that inclusion of the electric interaction term increases the theoretical value of the dressed moment of inertia  $I^*$  of a cyanide ion by about 20%.
- <sup>33</sup>A similar model has been previously proposed to describe the rotations of CO molecules embedded in an argon matrix [J. Manz, J. Am. Chem. Soc. **102**, 1801 (1980)]. One noteworthy difference, however, is that, in our model, the displacements of the neighboring lattice ions are derived quantities rather than assumed values.
- <sup>34</sup>Although we have left out of our picture the six (unknown) spring constants located between the cyanide dipole and the potassium ions, our final results would be *unchanged* by their inclusion, since the spring constants do not explicitly enter into the elastic coupling term in the expression for the angle-dependent moment of inertia.
- <sup>35</sup>The frequency extents of the roto-vibrational spectra for the nine hosts of interest (cf. Fig. 6) are much less than the corresponding maximum phonon frequencies of these hosts (cf. Ref. 26), even at RT. Hence, the adiabatic approximation should hold under all conditions investigated in this paper.
- <sup>36</sup>This is, of course, only an approximation, giving the lowest-order effect of the dressing.
- <sup>37</sup>Negligible changes in the fitted values of the rotational constants and the barrier parameter result if  $\gamma_0$  is constrained to be equal to  $\gamma_\infty$ , however.
- <sup>38</sup>N. W. Ashcroft and N. D. Mermin, *Solid State Physics* (Holt, Rinehart & Winston, Philadelphia, 1976), p. 465.
- <sup>39</sup>M. V. Klein, in *Physics of Color Centers*, edited by W. B. Fowler (Academic, New York, 1968), p. 529; B. Di Bartolo, *Optical Interactions in Solids* (Wiley, New York, 1968), Chap. 15, pp. 341–377. Note that this justifies our use of Lorentzian line shapes.
- <sup>40</sup>It is necessary to go through this rather elaborate procedure because the parameter  $s_{\text{dressed}}$  is very sensitive to the value of  $B_1^*$  (since varying  $B_1^*$  has the effect of changing the manifold width).
- <sup>41</sup>T. R. Gosnell, Ph.D. thesis, Cornell University, 1986 (unpublished), pp. 130–133.
- <sup>42</sup>If the 12 next-nearest-neighboring halide ions (with mass  $m_{\text{halide}}$ ) are included in the model, then it can be easily shown that the alkali ion mass ( $m_{\text{alkali}}$ ) in Eqs. (10) and (11) must be replaced by  $m_{\text{alkali}} + \frac{1}{2}m_{\text{halide}}$ , since the elastic coupling coefficient  $\xi_1$  falls off with the inverse square of the distance and the halide ions are a factor of  $\sqrt{2}$  farther away from the cyanide's position than are the alkali ions.
- <sup>43</sup>Interestingly enough, the values obtained by Callender and Pershan (Ref. 3) from their Raman data are in better agreement with our values than are those obtained in previous investigations, despite the fact that they found their values by using the Raman analogue of Seward and Narayananmurti's method. This fortuitous accord probably results both from the presence of a strongly allowed Q branch, which has the effect of artificially decreasing the peak-to-peak separations and secondly, from the fact that, in Raman spectra, the roto-vibrational lines are spaced twice as far apart as in ir spectra,

so that the overlap of adjacent lines will consequently be reduced. A reanalysis of the Raman spectra, in the spirit of our analyses of the ir spectra, would evidently be desirable. As an added bonus, the Raman data can give more than one value for  $B_0^*$  and it may be possible to interpret these values in the context of different angular components of the dressed moment of inertia.

<sup>44</sup>Conceivably there is a connection between the two, since  $\xi_1$  appears implicitly in both Eqs. (12) and (13).

<sup>45</sup>*American Institute of Physics Handbook*, edited by D. E. Gray (McGraw-Hill, New York, 1972), pp. 4-49 and 4-137.

<sup>46</sup>H. S. Sack and M. C. Moriarty, Solid State Commun. **3**, 93 (1965).

<sup>47</sup>M. Krantz and F. Lüty, Phys. Rev. B **37**, 7038 (1988).

<sup>48</sup>J. P. Hirth and J. Lothe, *Theory of Dislocations*, 2nd ed. (Wiley, New York, 1982), p. 42.

<sup>49</sup>E. R. Grannan, Ph.D thesis, Cornell University, 1989 (unpublished), p. 12.

<sup>50</sup>This equation is obtained by expanding Eq. (2-70) on p. 48 of J. P. Hirth and J. Lothe, *Theory of Dislocations*, Ref. 48.

<sup>51</sup>E. R. Grannan, M. Randeria, and J. P. Sethna, Phys. Rev. B **41**, 7784 (1990); **41**, 7799 (1990).

<sup>52</sup>A. S. Nowick and W. R. Heller, Adv. Phys. **12**, 251 (1963).

<sup>53</sup>J. K. Galt, Phys. Rev. **73**, 1460 (1948).

<sup>54</sup>Here we have used the so-called Voigt average. An alternative procedure (due to Reuss) consists in averaging over the elastic compliances. But performing the calculations, one obtains for  $(3\lambda + 5\mu)/(\lambda + 2\mu)$  the value 2.67 in the Voigt case

and 2.71 in the Reuss case, so that the two procedures give virtually identical results. One can similarly verify that one obtains  $\frac{8}{3}$ , to within a few percent, for *any* of the alkali halides.

<sup>55</sup>H. U. Beyeler, Phys. Rev. B **11**, 3078 (1975). Beyeler found that the values for the shape factors vary slightly depending on the crystallographic direction of the applied stress field. We ignore this effect for the sake of simplicity.

<sup>56</sup>Physically, the fact that the elastic displacements  $q_i$  do not explicitly depend on either the spring constants or the elastic constants of the system arises because the lattice is allowed to instantaneously relax about any given orientation of the cyanide ion. In an elastic approximation, this means that the nearest neighbors will take up positions which reflect the ellipsoidal shape of the dipole. In practice, of course, this is not quite correct and the displacements of the neighbors depend to some extent on the nature of the host, not just on the nature of the defect. This is reflected in the fact that the shape factor ( $\lambda_1 - \lambda_2$ ) for the cyanide ion varies slightly from host to host (cf. Table I), so that  $\xi_1$  depends *implicitly* on the elastic properties of the host.

<sup>57</sup>P. Sauer, Z. Phys. **194**, 360 (1966).

<sup>58</sup>S. L. Altmann and A. P. Cracknell, Rev. Mod. Phys. **37**, 19 (1965). There are several errors in their tables, the most serious of which occur for the  $E_g$  harmonics corresponding to  $J=8$  and 12.

<sup>59</sup>A. Sommerfeld, *Wave-Mechanics* (Methuen, London, 1930), p. 57.